

RESEARCH ARTICLE SUMMARY

CANCER IMMUNOTHERAPY

The tumor microenvironment underlies acquired resistance to CSF-1R inhibition in gliomas

Daniela F. Quail, Robert L. Bowman, Leila Akkari, Marsha L. Quick, Alberto J. Schuhmacher, Jason T. Huse, Eric C. Holland, James C. Sutton, Johanna A. Joyce*

INTRODUCTION: Therapies targeted against the tumor microenvironment (TME) represent a promising approach for treating cancer. This appeal arises in part from the decreased likelihood of acquired resistance through mutations in target TME cells, as is frequently observed with cancer cell-targeted therapies. Although classical mechanisms of tumor cell-intrinsic resistance to cytotoxic and targeted agents have been well-defined—including aberrant drug metabolism and transport, drug target mutation, and activation of alternative survival pathways—it still remains unclear whether resistance to TME-directed therapies follows similar principles. Given that TME-targeted agents are increasingly being evaluated in the clinic, it is becoming critical to mechanistically define how resistance may evolve in response to

these therapies in order to provide long-term disease management for patients.

RATIONALE: Macrophages and microglia are of the most abundant noncancerous cell types in glioblastoma multiforme (GBM), in some cases accounting for up to 30% of the total tumor composition. Macrophages accumulate with GBM progression and can be acutely targeted via inhibition of colony-stimulating factor-1 receptor (CSF-1R) to regress high-grade gliomas in animal models. However, it is currently unknown whether and how resistance emerges in response to sustained CSF-1R blockade in GBM. Despite this, multiple clinical trials are currently underway testing the efficacy of CSF-1R inhibition in glioma patients. Therefore, determining whether long-term CSF-1R inhibition can stably regress

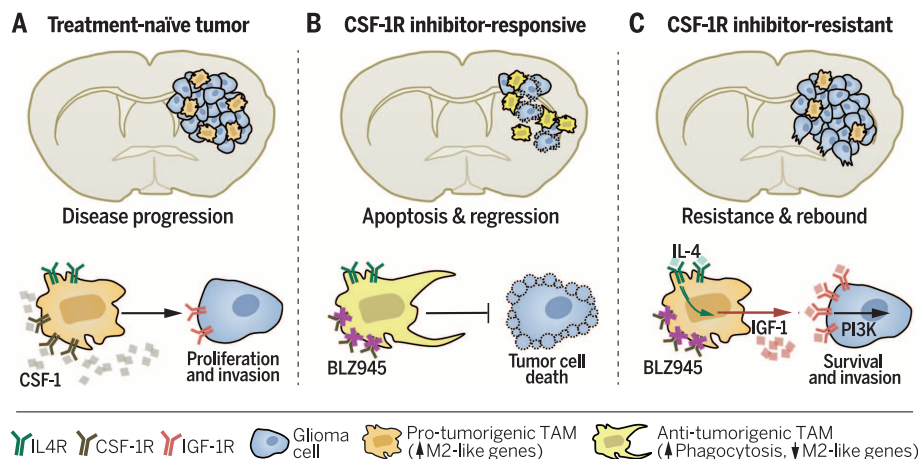
GBM by using animal models is an important and timely question to address.

RESULTS: Using genetic mouse models of GBM, we show that although overall survival is significantly prolonged in response to CSF-1R inhibition, tumors recur eventually in >50% of mice. Upon isolation and transplantation of recurrent tumor cells into naïve animals, gliomas reestablish sensitivity to CSF-1R inhibition, indicating that resistance is microenvironment-driven. Through RNA-sequencing of glioma cells and macrophages purified from treated tumors and ex vivo cell culture assays, we found elevated phosphatidylinositol 3-kinase (PI3K) pathway activity in recurrent GBM after CSF-1R inhibition, driven by macrophage-derived insulin-like growth factor-1 (IGF-1) and tumor cell IGF-1 receptor (IGF-1R). Consequently, combining IGF-1R or PI3K blockade with continuous CSF-1R inhibition in recurrent tumors significantly prolonged overall survival. In contrast, monotherapy with IGF-1R or PI3K inhibitors in rebound or treatment-naïve tumors

ON OUR WEBSITE
Read the full article at <http://dx.doi.org/10.1126/science.aad3018>

was less effective, indicating the necessity of combination therapy to expose PI3K signaling dependency in recurrent disease. Mechanistically, we found that activation of macrophages in recurrent tumors by IL4 led to elevated Stat6 and nuclear factor of activated T cells (NFAT) signaling upstream of IGF1, and inhibition of either of these pathways in vivo was sufficient to significantly extend survival.

CONCLUSION: We have identified a mechanism of drug resistance that can circumvent therapeutic response to a TME-targeted therapy and promote disease recurrence in the absence of tumor cell-intrinsic alterations. Specifically, we have uncovered a heterotypic paracrine signaling interaction that is initiated by the TME and drives resistance to CSF-1R inhibition through IGF-1R/PI3K signaling. Given that PI3K signaling is aberrantly activated in a substantial proportion of GBM patients, and that recent clinical trial results show limited efficacy in recurrent (albeit very advanced) GBM, it is possible that this pathway could similarly contribute to intrinsic resistance to CSF-1R inhibition. Our findings underscore the importance of bidirectional feedback between cancer cells and their microenvironment and support the notion that although stromal cells are less susceptible to genetic mutation than are cancer cells, a tumor can nonetheless acquire a resistant phenotype by exploiting its extracellular environment. ■



Resistance to CSF-1R inhibition in glioma. (A) Macrophages contribute to GBM progression by creating a protumorigenic niche associated with M2-like gene expression. CSF-1R is a critical receptor for macrophage biology and is under clinical evaluation as a therapeutic target in glioma. (B) Targeting CSF-1R early in gliomagenesis significantly prolongs survival in mouse models. CSF-1R inhibition reprograms macrophages to become antitumorigenic by down-regulating M2-like genes and enhancing phagocytosis. Tumor-derived survival factors sustain macrophage viability despite CSF-1R blockade. (C) After prolonged treatment, a subset of GBMs acquire resistance to CSF-1R inhibition, and tumors recur. This is driven by elevated macrophage-derived IGF-1 and high IGF-1R on tumor cells, resulting in PI3K pathway activation and enhanced glioma cell survival and invasion. Blocking this pathway and CSF-1R in preclinical trials yields a substantial survival benefit.

The list of author affiliations is available in the full article online.
*Corresponding author. Email: johanna@joycelab.org
Cite this article as D. F. Quail et al., *Science* 352, aad3018 (2016). DOI: 10.1126/science.aad3018

RESEARCH ARTICLE

CANCER IMMUNOTHERAPY

The tumor microenvironment underlies acquired resistance to CSF-1R inhibition in gliomas

Daniela F. Quail,¹ Robert L. Bowman,¹ Leila Akkari,^{1,2,3} Marsha L. Quick,¹ Alberto J. Schuhmacher,¹ Jason T. Huse,⁴ Eric C. Holland,⁵ James C. Sutton,⁶ Johanna A. Joyce^{1,2,3*}

Macrophages accumulate with glioblastoma multiforme (GBM) progression and can be targeted via inhibition of colony-stimulating factor-1 receptor (CSF-1R) to regress high-grade tumors in animal models of this cancer. However, whether and how resistance emerges in response to sustained CSF-1R blockade is unknown. We show that although overall survival is significantly prolonged, tumors recur in >50% of mice. Gliomas reestablish sensitivity to CSF-1R inhibition upon transplantation, indicating that resistance is tumor microenvironment-driven. Phosphatidylinositol 3-kinase (PI3K) pathway activity was elevated in recurrent GBM, driven by macrophage-derived insulin-like growth factor-1 (IGF-1) and tumor cell IGF-1 receptor (IGF-1R). Combining IGF-1R or PI3K blockade with CSF-1R inhibition in recurrent tumors significantly prolonged overall survival. Our findings thus reveal a potential therapeutic approach for treating resistance to CSF-1R inhibitors.

Therapies targeted against the tumor microenvironment (TME) represent a promising approach for treating cancer. This appeal arises in part from the decreased likelihood of acquired resistance through mutations in target TME cells, as is frequently observed with cancer cell-targeted therapies. Because multiple TME-directed therapies are currently advancing through different clinical trials (1, 2), this necessitates an understanding of potential mechanisms of intrinsic or acquired resistance. We have focused on addressing this issue by investigating whether resistance to a macrophage-targeted therapy emerges during the course of long-term trials in various preclinical models of high-grade glioma [glioblastoma multiforme (GBM)].

GBM is the most common and aggressive adult primary brain tumor, and survival is only minimally prolonged by current standard-of-care treatment, including surgery, radiation, and temozolomide chemotherapy (3). Accordingly, targeting the glioma TME is emerging as a promising al-

ternative therapeutic strategy. In GBM, tumor-associated macrophages and microglia (TAMs) comprise up to 30% of the bulk tumor mass (4). In many cancers, including glioma, elevated TAM numbers are associated with high-grade and poor patient prognosis (4–7). As such, targeting TAMs in GBM represents an attractive therapeutic approach.

Macrophages critically depend on colony-stimulating factor-1 (CSF-1) for multiple functions; consequently, strategies to target TAMs often include CSF-1 receptor (CSF-1R) blockade (8–10). In clinical trials, several approaches to inhibit CSF-1R are currently being used, including antibodies and small molecules (7, 11, 12). However, the long-term effects of these agents on clinical outcome are still under evaluation, and thus, gaining insight into potential mechanisms of drug resistance and/or inefficacy is now critical.

We used a potent and highly selective small-molecule CSF-1R inhibitor, BLZ945. We have shown that BLZ945 blocks early gliomagenesis, and that short-term treatment of advanced, high-grade glioma causes robust tumor debulking after just 7 days (8). CSF-1R inhibition has no direct effect on glioma cell viability because these cells do not express CSF-1R in the models we have used. Instead, glioma TAMs remain abundant and become antitumorigenic in response to treatment, by down-regulating markers of M2-like macrophage polarization/alternative activation and adopting a pronounced phagocytic phenotype (8). We address in this Research Article the unanswered question of whether long-term CSF-1R inhibition in aggressive late-stage GBM has a sus-

tainable antitumorigenic effect or instead leads to acquired resistance.

A subset of GBMs develop resistance to CSF-1R inhibition in long-term preclinical trials

We first analyzed the kinetics of GBM response to continuous long-term BLZ945 treatment using a transgenic platelet-derived growth factor-driven glioma (PDG) model (RCAS-hPDGF-B/Nestin-Tv-a; *Ink4a/Arf*^{-/-}) (Fig. 1A) (8, 13). Two weeks into the trial, we observed maximal tumor regression, with an average volume reduction of 62% (Fig. 1, B and C). At this time point, 8% of animals showed no evidence of residual tumor with magnetic resonance imaging (MRI). In contrast, vehicle-treated tumors exhibited a 2522% increase in volume over the same period (Fig. 1C).

After this regression phase, all BLZ945-treated tumors entered a dormancy phase, which lasted for ≥4 weeks (Fig. 1B). Of treated animals, 44% remained symptom-free and survived to the trial endpoint of 26 weeks ($P < 5 \times 10^{-17}$) (Fig. 1D) with minimal or, in some cases, no evidence of residual tumor as determined by MRI and histology (Fig. 1E). This is in stark contrast to vehicle-treated GBMs, which were purposely selected to be smaller in size upon treatment initiation (fig. S1A), yet median survival was only 15 days after treatment initiation (versus 93 days for BLZ945), and no animals survived beyond 6 weeks (Fig. 1D). After the dormancy phase observed in all BLZ945-treated animals, however, 56% eventually developed resistance, and tumors rebounded, despite effective, continued inhibition of CSF-1R phosphorylation in TAMs (Fig. 1, B and D, and fig. S1B).

We next focused on understanding how resistance to the CSF-1R inhibitor emerged and chose several time points throughout the long-term trial for comparison, including Veh [vehicle; 20% Captisol (Captisol, La Jolla, CA) until symptomatic], 7 days (BLZ945-responsive, regressing), 28 days (BLZ945-responsive, dormant), Reb (BLZ945-resistant, actively rebounding), and EP (26-week endpoint, stably regressed) (Fig. 1B). Histological analysis showed that after 7 days of BLZ945, tumor grade was substantially reduced. At 28 days and EP, histological grade remained low, with 33 and 50% of mice, respectively, showing no evidence of tumor via histology, and the remainder of animals exhibiting either residual disease or grade II tumors (fig. S1, C and D). By comparison, the majority of rebound tumors were grade III or IV and similar in size to Veh tumors at death (fig. S1, C to E). Both Veh and Reb tumors also exhibited a high proliferation:apoptosis index (Ki67:CC3), indicating a state of rapid growth (fig. S1F).

Glioma cells resistant to CSF-1R inhibition in vivo exhibit elevated phosphatidylinositol 3-kinase (PI3K) signaling

To determine the mechanism by which tumor cells acquire resistance, we first performed array comparative genomic hybridization (aCGH) analyses and found no copy number alterations in primary

¹Cancer Biology and Genetics Program, Memorial Sloan Kettering Cancer Center (MSKCC), New York, NY 10065, USA. ²Department of Oncology, University of Lausanne, CH-1066, Lausanne, Switzerland. ³Ludwig Institute for Cancer Research, University of Lausanne, CH-1066, Lausanne, Switzerland. ⁴Human Oncology and Pathogenesis Program, Memorial Sloan Kettering Cancer Center, New York, NY 10065, USA. ⁵Human Biology Division, Fred Hutchinson Cancer Research Center, Seattle, Washington, WA 98109, USA. ⁶Novartis Institutes for Biomedical Research, Emeryville, CA 94608, USA.

*Corresponding author. Email: johanna@joycelab.org

rebound glioma tumorsphere lines (fig. S2, passage 1). To then assess which signaling pathways are altered specifically in recurrent tumors, we first purified glioma cells (PDGFR α^+) from Veh, EP, and Reb lesions using fluorescence-activated cell sorting (FACS), and performed RNA-sequencing (RNA-seq). Glioma cells were isolated from EP lesions that were stably regressed but still detectable with MRI. Gene ontology analysis demonstrated that Veh and Reb tumor cells showed an enrichment of cell cycle-related genes, compared with EP tumor cells (fig. S3A), corroborating the observed changes in Ki67 levels (fig. S1F) and supporting the notion that EP tumors were in a state of cell-cycle dormancy. To interrogate which pathways were differentially regulated between the three groups, we used gene set variation analysis (GSVA) (14) for each pair-wise comparison. Nine gene sets in total were significantly enriched in Reb tumor cells as compared with EP (fig. S3B), including a PI3K gene set (Fig. 2A), potentially explaining the robust differences in proliferation given the importance of PI3K signaling in cell-cycle regulation. In accordance with this result, we found elevated phosphorylated (p)-Akt (a PI3K substrate) in Reb tissues as compared with that in Veh and EP, using immunofluorescence (IF) staining and Western blotting (Fig. 2B and fig. S3, C and D).

To investigate whether PI3K signaling is functionally important in driving recurrence, we performed a preclinical intervention trial. We treated PDG mice bearing high-grade gliomas with BLZ945 and imaged via MRI until they showed tumor rebound, at which point we intervened with BKM120 treatment (Fig. 2C, trial design 1, and fig. S3E) at an appropriate dose so as to avoid reported off-target effects (15). BKM120 was chosen because it is a brain-penetrant pan-Class 1 PI3K inhibitor that is currently being clinically evaluated in GBM patients with recurrent disease after standard therapy. Animals with rebound tumors treated with continued BLZ945 monotherapy led to a median survival of 13 days post-recurrence, whereas rebound tumors treated with BLZ945+BKM120 extended median survival to 51 days (Fig. 2D) and blocked tumor progression after 2 weeks of treatment (fig. S3F). In contrast, BKM120 monotherapy in rebound tumors (discontinued BLZ945) led to a median survival of 10 days, which was indistinguishable from the vehicle control (Fig. 2D). Moreover, BKM120 was only modestly effective in treatment-naïve tumors (fig. S3, G and H). Collectively, these results indicate that continued CSF-1R inhibition is necessary to expose PI3K signaling dependency in rebound tumors and, consequently, a heightened sensitivity to pathway inhibition.

To determine whether recurrence could be prevented by earlier PI3K inhibition, during the initial dormancy phase we treated GBM-bearing PDG mice with BLZ945 alone for 28 days, at which point we added BKM120 until the trial endpoint (Fig. 2C, trial design 2). With this early combination, the percentage of

animals that survived to endpoint increased substantially (91% BLZ945+BKM120) as compared with those given single-agent treatments (44% BLZ945 alone and 0% BKM120 alone) (Fig. 2E). Taken together, our results demonstrate that PI3K signaling is engaged during the acquisition of resistance to CSF-1R inhibition in the context of continued BLZ945 treatment.

Our finding that PI3K activation underlies resistance to CSF-1R inhibition was intriguing in light of the high frequency of mutations in the PI3K pathway in glioma patients (16). Therefore, we also investigated whether genetic mutations in PI3K/phosphatase and tensin homolog (PTEN) would similarly confer a resistance-like phenotype in mouse models, which could potentially be informative in the clinical setting. To address this question, we compared BLZ945 efficacy in two

additional RCAS-hPDGF-B/Nestin-Tv-a GBM models harboring distinct clinically relevant oncogenic alterations besides *Ink4a/Arf* loss, including *Pten* deletion (*Pten* KO model) or *p53* knockdown (*p53* KD model) (materials and methods). After 2 weeks of treatment, we found that BLZ945 efficacy in the *p53* KD model (56% reduction of tumor volume) was comparable with that of the PDG model (62% reduction). However, CSF-1R inhibition was less potent in the *Pten* KO model over the same time period (3% reduction) (Fig. 2F). Furthermore, although we did eventually observe a significant reduction in tumor volume in the *Pten* KO model after a prolonged treatment period of 4 weeks (11% reduction), this did not meet the response evaluation criteria in solid tumors (RECIST) standard for a partial response (Fig. 2G) (17). These results suggest that treatment efficacy of CSF-1R

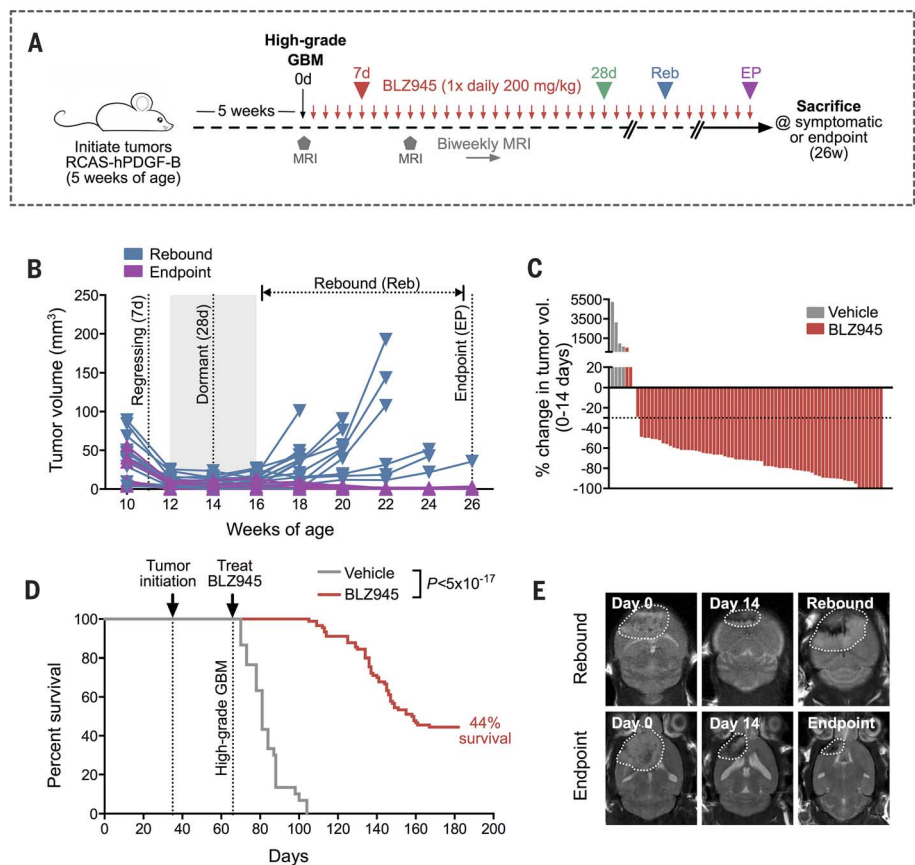


Fig. 1. Fifty-six percent of GBMs develop resistance to CSF-1R inhibition in long-term preclinical trials. (A) Long-term trial design for testing BLZ945 efficacy in the PDG model. High-grade PDG tumors were treated with BLZ945 (200 mg/kg/day) or vehicle (20% Captisol) and monitored with biweekly MRI for up to 26 weeks (defined endpoint; materials and methods) or until symptomatic. (B) Tumor volume curves from biweekly MRIs of long-term BLZ945 trials ($n = 90$ animals treated, 23 representative curves are shown). Four key phases are indicated, including 7 days (regressing tumor), 28 days (dormant tumor), Reb (recurrent tumor, evaluated on a mouse-to-mouse basis with MRI), and EP (stable regression at the 26-week endpoint). (C) Waterfall plots showing percent change in tumor volume between 0 and 14 days in a representative subset of animals from (D) (BLZ945, $n = 71$ mice; vehicle, $n = 4$ mice). (D) Kaplan-Meier of BLZ945-treated ($n = 90$) versus vehicle-treated ($n = 30$) mice bearing high-grade PDG tumors (Log-rank Mantel-Cox test, $P < 5 \times 10^{-17}$). Median survival for vehicle-treated animals was 15 days after treatment initiation, whereas median survival for BLZ945-treated animals was 93 days. (E) Representative MRI images over time of one mouse with a rebounded tumor (top row) and another mouse that had stable disease until EP (bottom row).

inhibitors may be blunted in patients with existing genetic alterations in the PTEN/PI3K pathway.

Resistance to CSF-1R inhibition is mediated by the microenvironment

We next investigated how PI3K was activated in rebound tumors and first explored whether resistance to BLZ945 was tumor cell-intrinsic or -extrinsic. We previously established that BLZ945 does not directly affect glioma cell lines in culture (8) and demonstrate here that CSF-1R inhibition also has no direct effect on viability of a panel of primary cell lines derived from rebound tumors (fig. S4A). We designed an intracranial tumor transplantation model using early-passage Reb cells in order to address the following hypotheses: (i) Resistance is tumor cell-intrinsic, therefore transplanted tumors will not respond to BLZ945, or (ii) resistance is mediated by the treatment-altered microenvironment, therefore transplanted tumors will reestablish sensitivity to CSF-1R inhibition in naïve animals. Transplanted rebound tumors responded to BLZ945 treatment in the naïve setting (Fig. 3A and fig. S4, B to F), indicating that resistance is likely mediated by the TME.

Fig. 2. Combined CSF-1R and PI3K inhibition improves survival in the PDG model. (A)

Gene set variation analysis based on RNA-seq from FACS-purified EP and Reb tumor cells (PDGFR α^+) (fig. S3B). Blue circles indicate gene sets significantly enriched in Reb tumor cells, and purple circles identify those enriched in EP tumor cells. The PI3K gene set is indicated with an arrow. Fold change is graphed as log₂(fold). Vertical dotted lines indicate fold cut-off for significance ($n = 5$ or 6 samples per group).

(B) Immunoblot from snap-frozen Veh, EP, and Reb tumors demonstrating elevated phospho (p)-AKT in Reb tumors compared with Veh and EP ($n = 3$ experiments, one representative blot is shown).

(C) Long-term trial design for evaluating BLZ945 and BKM120 combination therapy on PDG tumors. High-grade tumors were treated with BLZ945 until recurrent tumors developed (trial design 1) or until dormancy (28 days, trial design 2), whereupon BKM120 was either added (with continuous BLZ945 treatment) or switched (discontinued BLZ945).

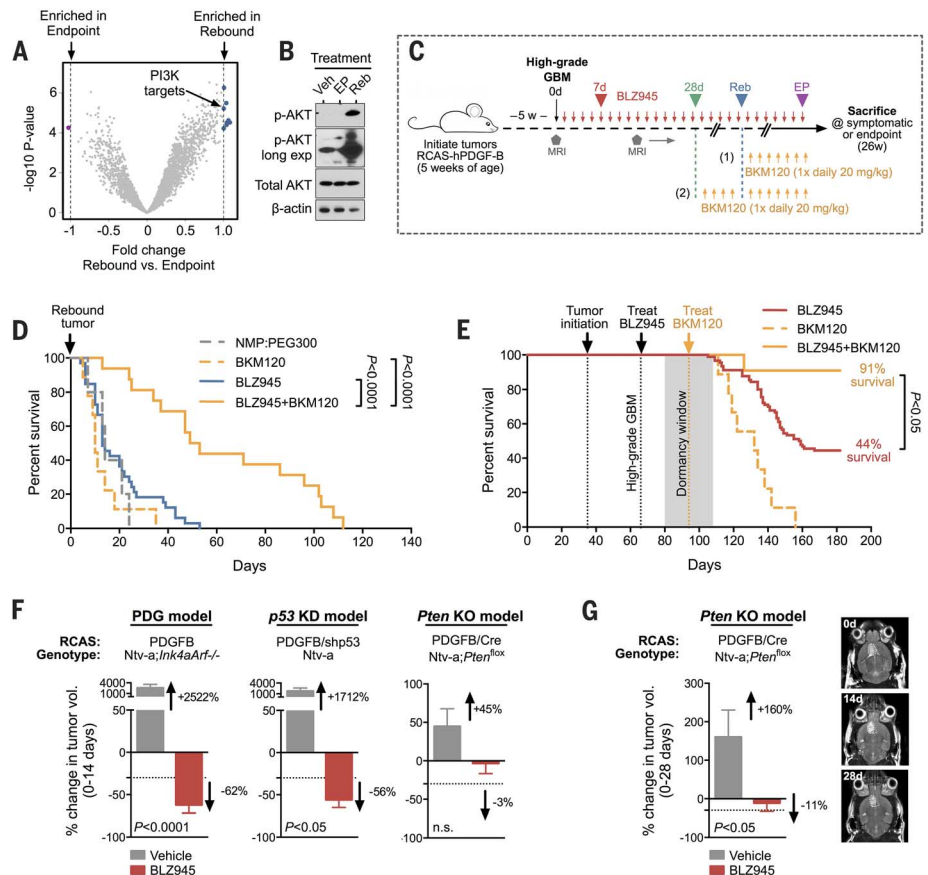
(D) Survival of animals with recurrent tumors treated either with BLZ945 alone ($n = 33$ mice), BKM120 alone ($n = 9$ mice), or BLZ945 in combination with BKM120 ($n = 16$ mice) (Fig. 2C, trial design 1). Combination of BLZ945+BKM120 led to an increase in overall survival (Log-rank Mantel-Cox test, $P < 0.0001$), and in median survival (51 days) after recurrence compared with BLZ945 (13 days) or BKM120 (10 days) monotherapy. (E) Survival of animals with 28-day dormant tumors treated either with BLZ945 alone ($n = 90$ mice; same cohort as presented in Fig. 1D), BKM120 alone ($n = 9$ mice), or BLZ945 in combination with BKM120 ($n = 11$ mice) (Fig. 2C, trial design 2). Combination of BLZ945+BKM120 led to increased overall survival compared with either monotherapy. Log-rank Mantel-Cox test was used to calculate significance. (F) Average percent change in tumor volume (0 to 14 days) between vehicle- or BLZ945-treated tumors, in three different RCAS-PDGFB-HA *Nestin-Tv-a* GBM models (termed PDG, *p53* KD, and *Pten* KO) (materials and methods). BLZ945 efficacy in the *p53* KD model (BLZ945, $n = 8$ mice; vehicle, $n = 6$ mice) was comparable with that of

We analyzed the TME in recurrent disease to determine how resistance to CSF-1R inhibition develops. We found that rebounding tumors always emerged adjacent to regions of glial scarring, characterized by reactive astrocytes, calcium deposition, and relatively low vascularity associated with elevated hypoxia (Fig. 3, B to D, and fig. S4, G to I). In contrast, scarring was infrequently observed in the 28-day and EP tumors (fig. S4I). The scar tissue architecture was reminiscent of gliosis in response to neurodegeneration or physical injury (18). Given the parallels between a wound-associated microenvironment and tumorigenesis in epithelial tissues (19), we hypothesized that this brain injury response may likewise be contributing to a microenvironment that is potentially triggering recurrent disease.

Rebound TAMs adopt a wound-associated signature driven by enhanced interleukin-4 (IL-4) signaling

During gliosis, activated macrophages play a central role in providing growth factors and signaling molecules to nearby astrocytes and neurons to form a reactive barrier that limits the extent of

tissue damage in the brain (18, 20). Given that BLZ945 is a macrophage-targeted drug, we analyzed TAM numbers and phenotype in rebound tumors. We have previously shown that TAMs are not depleted in the glioma TME in a 1-week trial with BLZ945, but rather down-regulate expression of M2-like genes and increase phagocytosis of tumor cells (8, 21). Consistently, we show here that TAMs are still present in 7-day, 28-day, EP, or Reb tumors (Fig. 3E and fig. S5A). When we used flow cytometry to discriminate between CD45^{lo}CD11b⁺ cells (putative microglia) versus CD45^{hi}CD11b⁺ cells [putative bone marrow-derived macrophages (BMDMs)] (22–24) in Veh, EP, and Reb tumors (materials and methods) (fig. S5B), we found that long-term BLZ945 treatment enriched for CD45^{lo}CD11b⁺ TAMs (fig. S5, C and D). This is potentially either a consequence of phenotypic mimicry between the macrophage populations or the result of one macrophage population responding differently to CSF-1R inhibition than the other. Costaining of CD68 or CD206 macrophage markers in combination with Ki67 demonstrated that a subset of remaining TAMs in rebound tumors were proliferating (fig. S5, E to



G). Although these results can only be formally confirmed with lineage tracing experiments, they at least suggest that rebound TAMs (enriched for CD45^{lo}CD11b⁺ cells) may undergo a low level of replication, presumably as a means to compensate for the duress caused by prolonged CSF-1R blockade.

To assess potential differences in activation states, we FACS-purified TAMs from Veh, EP, and Reb tumors and performed RNA-seq. Principal component analysis confirmed distinct global gene expression profiles for Veh, EP, and Reb TAMs (fig. S6A), and differential expression analysis revealed large numbers of differentially expressed genes between the three groups (table S1). We first focused on a subset of M2-like genes previously identified as altered by CSF-1R inhibition (8, 25). We found that compared with Veh TAMs, alternative activation was suppressed in EP TAMs, whereas a subset of these genes were highly expressed in Reb TAMs (Fig. 3F). In ac-

cordance with previous findings (8), no inverse relationship was observed for M1-like markers such as tumor necrosis factor- α (TNF α) across the different treatment groups (25). Together, these findings support our hypothesis that the Reb TME is protumorigenic.

Given the similarities in alternative activation between Veh and Reb TAMs according to the M1/M2-like paradigm (26), yet clear differences in drug response between treatment-naïve and rebound tumors, we next used a more fine-tuned approach to defining macrophage phenotype. We computationally interrogated a spectrum model of macrophage activation, defined by gene sets that are altered in response to different stimuli, including interferon- γ (IFN- γ), IL4, TNF α , transforming growth factor- β 1 (TGF β 1), IL1 β , and two Toll-like receptor (TLR) agonists specific for TLR2 [macrophage-activating lipopeptide 2 (MALP2)] and TLR9 [unmethylated CpG-containing oligonucleotide (CPG)] (27, 28). We determined that

IL4- and TGF β 1-targeted gene sets were significantly enriched in Reb TAMs compared with Veh TAMs (Fig. 4A) and also found a significant enrichment of these same gene sets in Reb TAMs versus EP TAMs (Fig. 4B). Given that IL4 is a known mediator of alternative activation associated with a wound-healing phenotype in macrophages (20, 29), and the role of TGF β 1 during wound-healing and tissue turnover in multiple contexts (30, 31), these results were consistent with our observation of glial scarring in association with rebound tumors. Indeed, a number of M2-like genes expressed by macrophages involved in wound repair and resolving inflammation (*Retnla*, *Chil3*, and *Ccl17*) were enriched in Reb TAMs (Fig. 3F). In contrast, RNA-seq analyses of an independent set of Reb and 28-day TAM samples revealed no significant differences in expression across this same gene set (fig. S6B), suggesting that a subset of 28-day tumors may be rebound precursors, and that induction of M2-like gene

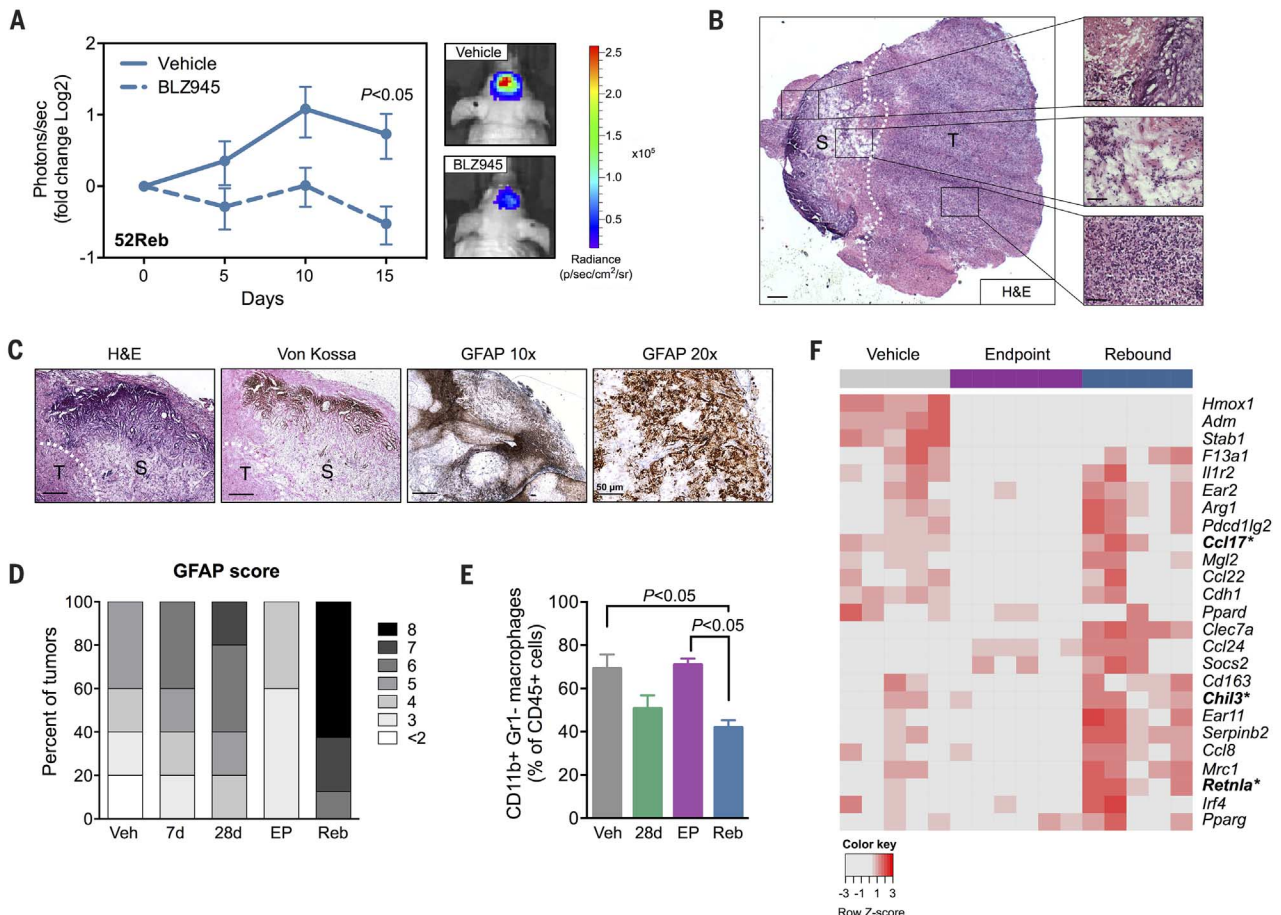


Fig. 3. Resistance to CSF-1R inhibition is mediated by the microenvironment and rebound TAMs are alternatively activated. (A) Quantification of BLI from intracranially transplanted 52Reb cells into naïve mice. Results show that 52Reb cells, isolated from a recurrent PDG tumor that developed resistance to BLZ945 treatment in vivo, reestablish sensitivity to BLZ945 in the naïve setting (Student's *t* test day 15, $P < 0.05$, $n = 10$ mice). Representative BLI images at day 15 are shown. (B) (Left) H&E (hematoxylin and eosin) of a rebound tumor (T) adjacent to glial scarring (S). Scale bar, 500 μ m. (Right) Representative regions of calcification (top), reactive astrocytic barrier (middle), and recurrent tumor (bottom). Scale

bars, 50 μ m. (C) H&E, Von Kossa, and GFAP (glial fibrillary acidic protein) staining on rebound tissue. Scale bars, 200 μ m; except GFAP, 20 \times = 50 μ m, as indicated. (D) Allred score for the astrocyte marker GFAP, showing a higher intensity and proportion of GFAP⁺ staining in Reb tissues ($n = 8$ mice) compared with other treatment groups ($n = 5$ mice per group). (E) Flow cytometry of TAMs (CD45⁺CD11b⁺Gr1⁻) in Veh, 28-day, EP, and Reb tumors ($n = 5$ to 7 tumors). Data were analyzed with a one-way ANOVA and Tukey's multiple comparisons test. (F) Heatmap showing RNA-seq expression changes of M2-like associated genes in Veh, EP, and Reb TAMs ($n = 5$ or 6 per group). Wound-associated genes are indicated in bold with asterisks.

expression precedes recurrence. When we investigated the ability of IL4 or TGF β 1 to regulate expression of these wound-associated genes in BMDMs in vitro, we found that IL4 was a potent inducer, whereas TGF β 1 was not (Fig. 4C and fig. S6, C and D), indicating the specificity of IL4 for regulation of this particular gene set. Corroborating these findings, we confirmed increased expression of *Il4* in rebound tumors by means of quantitative reverse transcription polymerase chain reaction (RT-PCR) (Fig. 4D) and elevated canonical downstream signaling by means of immunofluorescent staining for phosphorylated Stat6 (p-Stat6) in PDG tissue samples from the long-term trials (fig. S6, E and F). These results do not exclude the possibility that TGF β may be playing a role in rebound tumors that is distinct from, or indirectly connected to, alternative activation of TAMs.

To determine the cellular source of IL4 in our model, we used multicolor flow cytometry to immunoprofile Veh, EP, and Reb tumors using a panel of myeloid [CD11b, Gr1, Ly6G, Ly6C, CD11c, Tie2, and major histocompatibility complex (MHC II)] and lymphoid (CD19, CD3, CD4, CD8, and FoxP3) cell markers. Although we found few cell types that were specifically enriched in rebound tumors (fig. S7, A to G), there was a significant increase in the proportion of CD3 $^+$ T cells in rebound tumors, driven by the CD8 $^+$ fraction (Fig.

4, E and F). FACS-purification of these cells from rebound tumors along with other putative contributors of IL4 [including astrocytes (Fig. 3D), B cells (32–34), and bulk T cells] revealed that *Il4* expression was enriched in both bulk T and CD8 $^+$ T cell fractions (Fig. 4G and fig. S7H). In comparison, expression of *Il13*, a closely related cytokine that shares the IL4R α subunit in its heterotypic receptor to initiate canonical Stat6 signaling, was enriched in the bulk T cell fraction (Fig. 4G). Expression of *Il4* was assessed in a panel of human cell types and detected in CD8 $^+$ T cells as expected, in addition to monocytes, eosinophils, astrocytes, and brain microvascular cells (fig. S7I). Although additional analyses are needed to establish the precise cellular source of these cytokines in brain malignancies in patients, our data are consistent with IL4 being produced by multiple cell types.

The IGF-1/IGF-1R signaling axis is induced in rebound gliomas

We next investigated how IL4 and wound-associated gene expression might be connected to PI3K signaling in rebound tumors. Differential gene expression analysis revealed that TAM-derived *Igf1* was one of the most significantly up-regulated genes in Reb TAMs compared with EP TAMs, which we confirmed in comparisons with Veh TAMs or 28-day TAMs (Fig. 5, A and

B, fig. S8A, and table S1). This was particularly interesting because *Igf1* is an IL4 target gene in macrophages (fig. S8B) (35–37), it is a known mediator of tissue repair and neuroprotection (38–41), and one of its canonical downstream signaling pathways is PI3K/Akt (42). Congruent *Igf1r* up-regulation was identified in glioma cells purified from rebound tumors (Fig. 5C and table S1), elevated p-IGF-1R was found in rebound tumors by means of immunostaining and Western blotting (Fig. 5D and fig. S8, C and D), and *Igf1* up-regulation was found in snap-frozen rebound tissue samples by means of quantitative RT-PCR (fig. S8E). Additionally, levels of *Igf1* expression were substantially higher in Reb TAMs than tumor cells, whereas *Igf1r* expression was enriched in tumor cells as compared with TAMs (fig. S8F). Together, these data demonstrate elevated IGF-1 signaling in recurrent disease.

To assay the effects of IGF-1 specific to the rebound setting, we used multiple approaches: First, through Western blot analysis, we confirmed higher baseline levels of p-IGF-1R in early-passage rebound tumor cell lines as compared with cell lines that we were able to propagate from dormant tumors in culture (materials and methods) (fig. S8G). We determined that phosphorylation and downstream signaling could be reduced in rebound cell lines by using an inhibitor of IGF-1R (fig. S8G) and that early-passage rebound cells were more sensitive

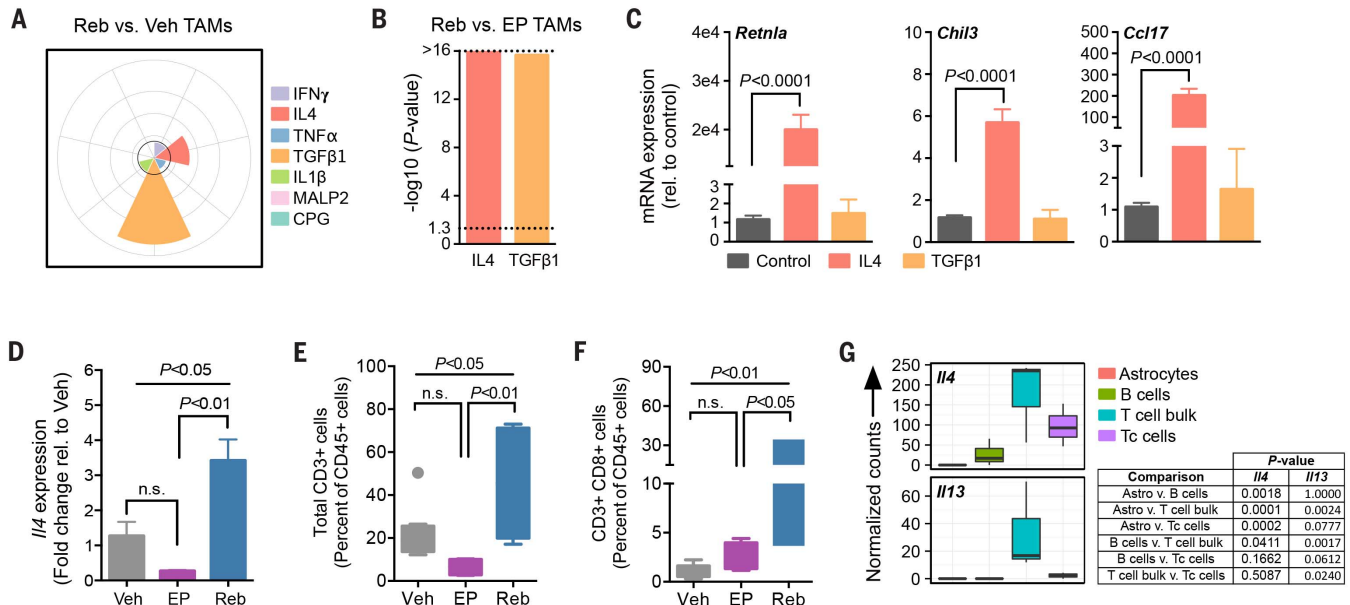


Fig. 4. IL4 activates wound-associated genes in rebound TAMs and is produced by T cells in the rebound tumor microenvironment. (A) Spectrum model of macrophage activation by using GSEA of transcriptional programs regulated by the indicated cytokines (materials and methods). Reb TAMs exhibit activation of programs driven by TGF β 1 and IL4 compared with Veh TAMs ($n = 5$ mice per group). The $-\log_{10}$ (P value) is plotted for each gene set (0, 4, 8, 12, and >16 , radially outward in gray concentric circles). The black circle indicates a $-\log_{10}$ (P value) cutoff of 3. (B) GSEA as in (A), confirming that Reb TAMs exhibit activation of programs driven by IL4 and TGF β 1 compared with EP TAMs ($n = 5$ or 6 mice per group). Dotted line demarcates $P < 0.05$. (C) Quantitative RT-PCR analysis demonstrates that IL4 induces expression of the wound-associated genes *Retnla*, *Chil3*, and *Ccl17* in BMDMs in culture, whereas recom-

binant TGF β 1 treatment does not. Bone marrow isolate was obtained from five or more independent WT mice for replicate experiments. (D) Quantitative RT-PCR analysis of *Il4* expression in snap-frozen whole-tumor samples from Veh, EP, or Reb treatment groups, demonstrating elevated expression in the Reb setting ($n = 4$ tumors) compared with both Veh ($n = 4$ tumors) and EP ($n = 4$ tumors). (E) Flow cytometry of total CD3 $^+$ T cells ($n = 5$ to 10 tumors) and (F) CD3 $^+$ CD8 $^+$ cytotoxic T cells ($n = 5$ to 10 tumors) in Veh, EP, and Reb tumors. (G) RNA-seq data from a panel of cell types [GFAP $^+$ astrocytes, CD19 $^+$ B cells, CD3 $^+$ CD8 $^+$ cytotoxic T cells (Tc), and remaining CD3 $^+$ CD8 $^-$ bulk T cells] isolated from Reb tumors by means of FACS ($n = 3$ tumors). Results show elevated *Il4* expression in bulk T and Tc cells, and *Il13* expression in bulk T cells. Significance values for (C) to (F) were calculated with one-way ANOVA and Tukey's multiple comparisons test.

to IGF-1R blockade than were naïve glioma cells in vitro by using multiple pharmacological inhibitors (Fig. 5E and fig. S8H).

Next, to model the effects of macrophage-derived IGF-1 on rebound tumor cells, we designed an ex vivo culture system using primary

glioma microenvironment cultures (GMECs). GMECs contain multiple cell types from the glioma TME when harvested at early passage, including macrophages, T cells, and astrocytes, among others (fig. S8I) (8). We hypothesized that rebound GMECs would be able to stimulate pro-

duction of IGF-1 by macrophages and subsequent growth of tumor cells. To test this, we collected conditioned media (CM) from rebound GMECs and applied it to wild-type (WT) BMDMs for 24 hours. After this treatment, we collected CM from the GMEC-stimulated BMDMs (Stim CM)

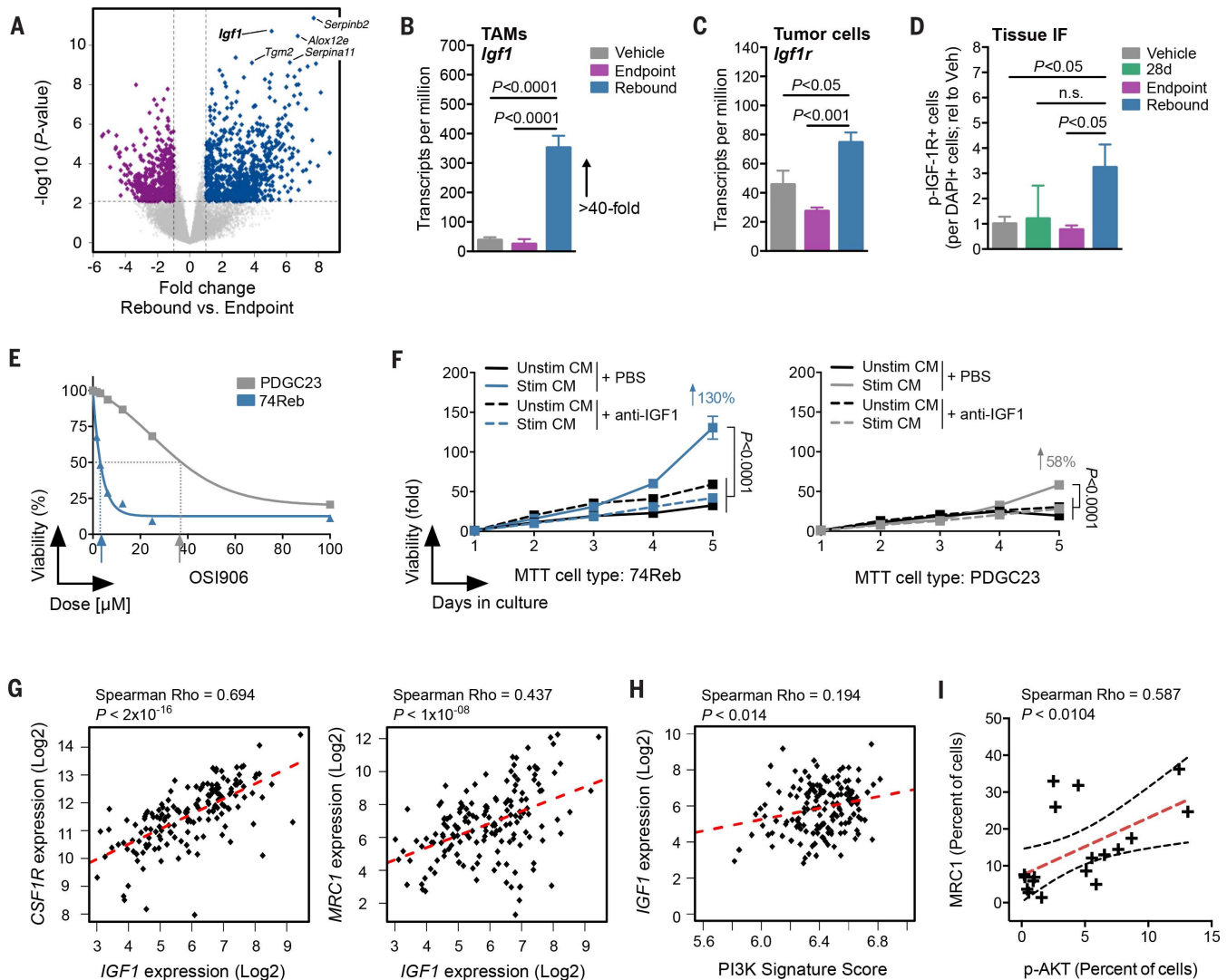


Fig. 5. The IGF-1/IGF-1R axis is induced in rebound gliomas. (A) Volcano plot showing the fold change [$\log_2(\text{fold})$] between Reb ($n = 5$ tumors) and EP ($n = 6$ tumors) TAMs on the x axis and the significance [$-\log_{10}(P \text{ value})$] on the y axis. Blue dots indicate genes up-regulated in Reb TAMs, whereas purple dots indicate genes down-regulated in Reb TAMs. *Igf1* is labeled in the top right quadrant. (B) RNA-seq barplot depicting *Igf1* transcripts per million (TPM) in Veh, EP, and Reb TAMs ($n = 5$ or 6 tumors per group; one-way ANOVA and Tukey's multiple comparisons). (C) RNA-seq barplot depicting *Igf1r* TPM in Veh, EP, and Reb tumor cells ($n = 5$ or 6 tumors per group; one-way ANOVA and Tukey's multiple comparisons). (D) Quantification of immunofluorescent staining of phospho (p)-IGF-1R in Veh, 28-day, EP, and Reb tumor tissues. Results show pIGF-1R is elevated in rebound tumors compared with all other groups ($n = 5$ to 8 tumors per group; one-way ANOVA and Dunnett's multiple comparisons to Reb). (E) MTT assay demonstrating higher sensitivity of an early-passage primary rebound PDG cell line (74Reb, blue) to IGF-1R inhibition with OSI906 compared with a primary treatment-naïve PDG cell line (PDGC23, gray) ($n = 3$ independent replicates, one representative experiment shown). IC_{50} values are indicated with arrows. (F) MTT proliferation assays of 74Reb

cells (left) compared with PDGC23 cells (right), treated with conditioned media (CM) from BMDMs that were stimulated with rebound glioma microenvironment culture CM (fig. S8, I and J). Stimulated BMDM CM (Stim CM) induced growth of 74Reb cells more than PDGC23 cells (130 versus 58%, respectively), and this effect was blocked with an anti-IGF-1 neutralizing antibody ($n = 4$ replicate experiments). A one-way ANOVA and Dunnett's multiple comparisons with Stim CM + PBS was used to calculate differences at 5 days ($P < 0.0001$ for all). (G) Correlation between *IGF1* and *CSF1R* or *MRC1* expression from TCGA-GBM data. (H) Single sample GSEA for a hallmark PI3K signature was used to assign a pathway activity score (materials and methods) across patients from the TCGA-GBM data set. PI3K signature scores were then correlated with *IGF1* expression levels as shown. (I) Linear regression analysis of immunohistochemical staining for phospho (p)-AKT and MRC1 in serial sections from GBM patient tissue ($n = 18$ patients). A significant correlation between MRC1 protein levels and AKT signaling was observed. For correlational analyses [(G) to (I)], a Spearman coefficient was used to assess significance, and a line of best fit is shown (dashed red). The 95% confidence band (dashed black) is also shown in (I).

and applied it to either rebound or naïve tumor cell lines in an MTT assay, plus or minus a neutralizing antibody against IGF-1 (experimental design is provided in fig. S8J). We found that Stim CM induced proliferation of rebound cell lines more effectively than naïve cell lines, and this effect was blocked by IGF-1 neutralization (Fig. 5F). These results suggest that the cells within a recurrent tumor are capable of stimulating production of IGF-1 by macrophages, which in turn gives a proliferative advantage to rebound tumor cells.

To assess the relevance of the IGF-1/IGF-1R axis in human malignancy, we evaluated *IGF1* expression in publicly available human GBM gene expression data sets. We found that *IGF1* expression was significantly correlated with macrophage-specific genes (*CSF1R*, *CD68*, and *AIF1*) and with genes associated with an M2-like

phenotype (*CD163* and *MRC1*) in The Cancer Genome Atlas (TCGA) GBM samples (Fig. 5G and fig. S9A). No such correlations were found for genes enriched in astrocytes (*GFAP* and *ALDH1L1*) (fig. S9A), another key cell type in the glial scar phenotype (18). We also confirmed that *IGF1* expression was significantly correlated with a PI3K signature score (Fig. 5H) generated from single sample gene set enrichment analysis (GSEA) for hallmarks of PI3K signaling (43). Consistently, immunohistochemistry (IHC) quantitation on an independent set of human GBM tissue samples revealed a significant association between p-AKT and the M2-associated protein MRC1 (Fig. 5I, fig. S9B, and table S2). Together, these data support our hypothesis that high IGF-1 levels translate to elevated PI3K signaling in patients, and that this axis is associated with M2-like gene expression.

To determine whether macrophages are the predominant source of *IGF1* in humans, we used quantitative RT-PCR to show that macrophages express high levels of *IGF1* compared with that in different immune cell types, astrocytes, endothelial cells, and glioma cells (fig. S9C). Consistently, we found that *IGF1* expression was enriched in TAMs compared with the tumor bulk in GBM (fig. S9D) (44), and in mesenchymal GBM compared with other molecular subtypes (fig. S9E) in which high macrophage content is a hallmark histological feature. These data corroborate our findings in the PDG model by suggesting that macrophages are an important source of *IGF1* in human malignancy.

Last, we used publicly available data sets to assess survival correlations in patients. We first generated Kaplan Meier curves using a median cutoff for *IGF1* expression levels and found no significant difference in overall survival between

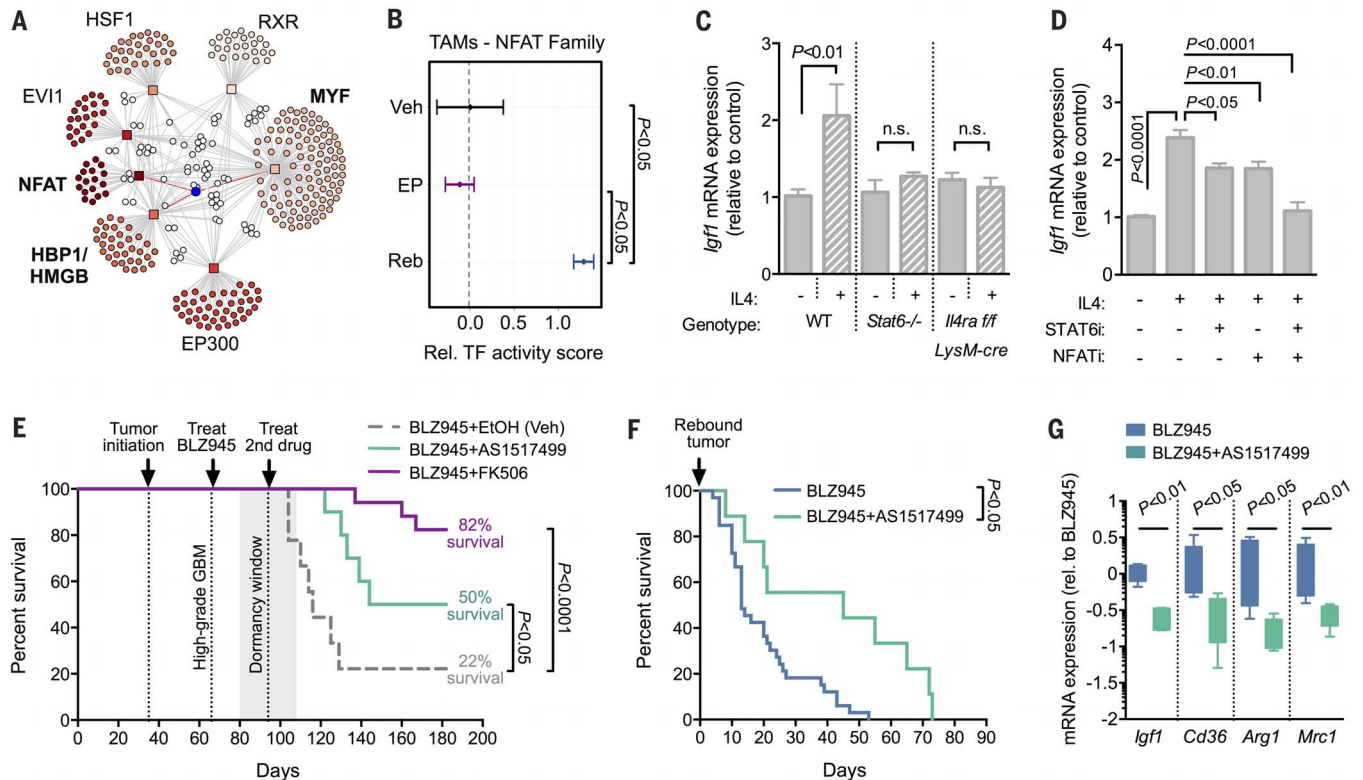


Fig. 6. NFAT and Stat6 cooperate to regulate *Igf1* expression in rebound TAMs. (A) Transcription factor (TF) network analysis from RNA-seq data showing enriched TF families (squares) connected with a line to target genes (circles). White circles indicate genes targeted by multiple TFs. *Igf1* is shown as a blue circle connected by red lines to three regulating TF families. (B) Predicted NFAT TF activity in Veh, EP, and Reb TAMs, showing a high score specifically in Reb TAMs ($n = 5$ or 6 tumors per group). (C) Quantitative RT-PCR analysis of *Igf1* in BMDMs derived from WT, *Stat6*^{-/-}, or *Il4ra flox*; *LysM-cre* mice, treated \pm recombinant mouse IL4 (10 ng/ml; $n = 5$ independent experiments). Student's *t* test was used for pairwise comparisons within each genotype. (D) Quantitative RT-PCR analysis of *Igf1* in BMDMs derived from WT mice, treated \pm recombinant mouse IL4 (10 ng/ml), a Stat6 inhibitor (AS1517499, 50 nM), and/or an NFAT inhibitor (INCA-6, 40 μ M; $n = 6$ independent experiments). A one-way ANOVA and Dunnett's multiple comparisons with the +IL4 condition was used to calculate significance. (E) Survival of PDG animals with high-grade tumors treated first with BLZ945 alone until dormancy (28 days) and

then enrolled on combination therapy with either AS1517499 ($n = 10$ mice), FK506 (NFAT inhibitor; $n = 17$ mice), or EtOH vehicle control ($n = 9$ mice). Combination therapy with either inhibitor led to a significant increase in overall survival (FK506, 82% survival, $P < 0.0001$; AS1517499, 50% survival, $P < 0.05$), compared with vehicle control (22% survival). Log-rank Mantel-Cox test was used to calculate significance. (F) Survival curve representing animals with recurrent tumors treated either with continuous BLZ945 alone ($n = 33$ mice) or BLZ945+AS1517499 ($n = 9$ mice). Combination therapy led to a significant increase in overall survival (Log-rank Mantel-Cox test, $P < 0.05$), and in median survival after recurrence (45 days) compared with BLZ945 monotherapy (13 days). (G) Quantitative RT-PCR analysis of *Igf1*, *CD36*, *Arg1*, and *Mrc1* levels in a subset of animals from (F). Results show a significant reduction of *Igf1* expression in rebound tumors after Stat6 inhibition ($n = 5$ mice per group, $P < 0.01$), and a reduction of known IL4-Stat6 transcriptional targets (*CD36*, $P < 0.05$; *Arg1*, $P < 0.05$; *Mrc1*, $P < 0.01$), confirming drug efficacy in the brain (Mann-Whitney test).

IGF1^{high} and *IGF1^{low}* patients (fig. S9F). Given that baseline IGF-1 signaling is critical during normal homeostasis in the brain (41), and also the extremely rapid progression of GBM in patients, we also surveyed the top 10% of *IGF1^{high}* patients (versus all remaining) and found a clear decrease in overall survival (fig. S9F). When we used this same stringent top-10% cutoff for a macrophage marker (*AIF1*; also known as *Iba1* in mouse) that correlates significantly with *IGF1* expression levels (fig. S9A), there was no separation of survival curves (fig. S9F), suggesting that differences in survival are not simply due to differences in macrophage abundance, but rather to differences in degree of *IGF1* expression.

NFAT and Stat6 cooperate to regulate *Igf1* expression in rebound TAMs

We next used transcription factor (TF) activity analysis to identify putative transcriptional networks regulating *Igf1* expression in rebound tu-

mors. Seven TF families showed enriched activity in Reb TAMs compared with EP TAMs (Fig. 6A, fig. S10A, and table S3). Three of these were found to regulate *Igf1* [nuclear factor of activated T cells (NFAT), MYF, and HMGB families] (Fig. 6A), of which the NFAT family showed enriched activity specifically in Reb TAMs compared with both EP and Veh TAMs (Fig. 6B). These results were particularly interesting given the cooperative relationship between NFAT and Stat6 (canonical IL4 pathway) in transcriptional regulation (45). Corroborating these results, we found that IL4, but not TGF β 1, induced *Igf1* expression in BMDMs in vitro, which was reduced by an NFAT inhibitor (fig. S10B).

To further characterize the role of IL4-induced NFAT and/or Stat6 signaling in *Igf1* regulation, we performed a series of in vitro and in vivo experiments. First, we confirmed that IL4 strongly induced expression of *Igf1* and the three representative alternative activation/wound-associated

genes (*Retna*, *Chil3*, and *Ccl17*) in WT BMDMs, and that this capacity was reduced in BMDMs from either *Stat6^{-/-}* or *Il4ra flox*; *LysM-cre* mice (Fig. 6C and fig. S10C). Furthermore, whereas pharmacological inhibition of either Stat6 or NFAT partially reversed the effects of IL4 on *Igf1*, *Retna*, *Chil3*, and *Ccl17* expression, dual inhibition of these pathways in WT BMDMs completely blocked the effects of IL4 on this gene set (Fig. 6D and fig. S10D). To validate the importance of these pathways in vivo, PDG mice with high-grade GBMs were treated continuously with BLZ945 alone until 28 days, at which point FK506 (a NFAT-calcineurin inhibitor) or ASI1517499 (a Stat6 inhibitor) was added until the trial endpoint. With addition of either of these inhibitors, the percentage of animals that survived to endpoint was significantly increased (22% BLZ945+Veh, 50% BLZ945+ASI1517499, and 82% BLZ945+FK506) (Fig. 6E). In accordance with these results, when we treated animals with ASI1517499 in combination

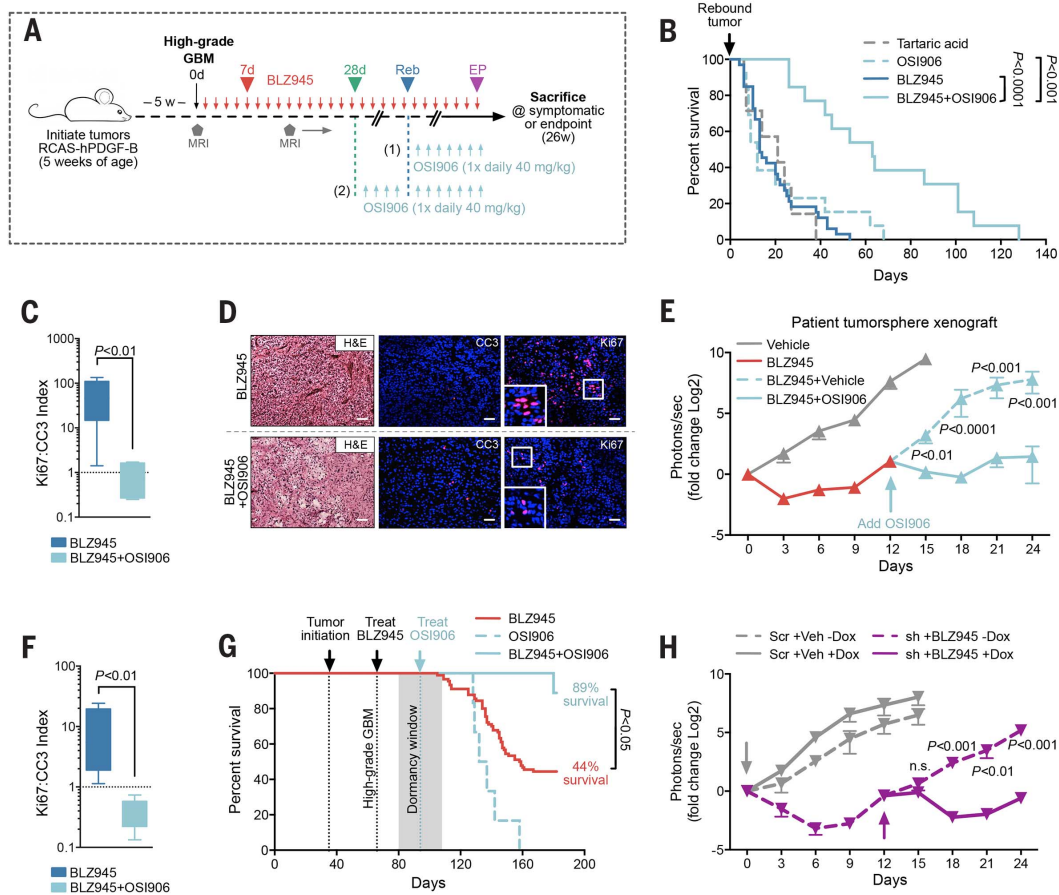


Fig. 7. Combination of CSF-1R inhibition and IGF-1R inhibition significantly improves outcome in preclinical models.

(A) Long-term trial design for testing BLZ945 and OSI906 combination therapy on PDG tumors. High-grade tumors were treated with BLZ945 until recurrent tumors developed (trial design 1) or until dormancy (28 days, trial design 2), when OSI906 was either added (with continuous BLZ945) or switched (discontinued BLZ945). (B) Survival of animals with recurrent tumors treated either with BLZ945 alone ($n = 33$ mice), OSI906 alone ($n = 13$ mice), or BLZ945 in combination with OSI906 ($n = 13$ mice) (Fig. 7A, trial design 1). Combination therapy of BLZ945+OSI906 led to an increase in overall survival (Log-rank Mantel-Cox test, $P < 0.001$), and in median survival after recurrence (63 days) compared with BLZ945 (13 days) or OSI906 (12 days) monotherapy. (C) Ki67:CC3 (cleaved caspase 3) proliferation:apoptosis index from immunofluorescent staining of recurrent tumors treated with BLZ945 alone versus BLZ945+OSI906 for 2 weeks (Mann-Whitney test, $P < 0.01$, $n = 7$ or 8 mice). (D) Representative H&E and immunofluorescent images corresponding

to data in (C). Scale bars, 50 μ m. (E) BLI from orthotopically xenografted patient-derived tumorspheres (TS573) that were subject to 24 days of treatment with BLZ945 (red) versus vehicle control (gray). Results demonstrate that treatment with BLZ945+OSI906 blunts outgrowth of rebound tumors compared with BLZ945+vehicle. Mann-Whitney test was used to calculate P values for each time point ($n = 5$ to 20 mice). (F) Ki67:CC3 index from immunofluorescent staining of TS573 orthotopic xenograft tissues (Mann-Whitney test, $P < 0.01$, $n = 5$ mice per group). (G) Kaplan-Meier analysis of PDG animals treated either with BLZ945 alone ($n = 90$ mice; same cohort as presented in Fig. 1D), OSI906 alone ($n = 6$ mice), or with BLZ945 in combination with OSI906 during dormancy ($n = 9$ mice) (Fig. 7A, trial design 2). Combination therapy of BLZ945+OSI906 extended overall survival compared with either monotherapy. Log-rank Mantel-Cox test was used to calculate significance. (H) BLI of orthotopically xenografted U251 cells genetically engineered to express an *IGF1R*-targeted dox-inducible shRNA (sh; $n = 15$ or 16 mice; purple lines) or a scrambled control vector (Scr; $n = 4$ or 5 mice; gray lines). Colored arrows indicate respective administration of dox. Graph shows two combined shRNAs; data for individual hairpins are shown in fig. S13E. Mann-Whitney test was used to calculate significance.

with continued BLZ945 treatment at a later time point, during the rebound phase we were able to extend survival (Fig. 6F), and quantitative RT-PCR analysis of these tumors confirmed reduced levels of *Igf1* expression along with additional known targets of IL4-Stat6 signaling (*CD36*, *Arg1*, and *Mrc1*) (Fig. 6G) (27). Collectively, these data suggest that both NFAT and/or Stat6 signaling contribute to macrophage activation and IGF-1 regulation in rebound tumors, and that pharmacological blockade of either of these pathways is sufficient to reduce the incidence of disease recurrence. However, these models are limited by their inability to distinguish cell type-specific pathway blockade. Furthermore, although FK506 is used in multiple clinical settings, targeted specificity of the Stat6 inhibitor *in vivo* is not fully characterized. In future studies, elucidating the effects of T cell-specific IL4 expression, or macrophage IL4R, on BLZ945 efficacy through the use of genetic models would provide additional insight into mechanistic communication between different TME cell types.

Combination of CSF-1R and IGF-1R inhibition improves outcome

To formally test our hypothesis that the IGF-1/IGF-1R axis may underlie resistance to CSF-1R inhibition, we targeted IGF-1R *in vivo* using both pharmacological and genetic approaches. First, we designed similar preclinical intervention trials as for BKM120, except with an inhibitor of IGF-1R (OSI906/Linsitinib). We treated PDG mice with BLZ945 until they showed signs of rebound as seen with MRI, at which point we intervened with OSI906 (Fig. 7A, trial design 1). OSI906 was chosen because it is currently being clinically evaluated for multiple cancer types, its effect on BMDM viability *in vitro* was minimal compared with other IGF-1R inhibitors tested (fig. S11A), and we confirmed that it is brain-penetrant in rebound tumors by showing reduced p-IGF-1R immunostaining (fig. S11B). In concordance with the BLZ945+BKM120 trial results, we found that rebound tumors treated with OSI906 and continuous BLZ945 significantly extended median survival to 63 days (versus 13 days after recurrence for continuous BLZ945 monotherapy) (Fig. 7B), and markedly reduced tumor progression and proliferation:apoptosis ratios after 2 weeks of treatment (Fig. 7, C and D, and fig. S11C). In contrast, OSI906 monotherapy in rebound tumors (discontinued BLZ945) led to a median survival of just 12 days (Fig. 7B) and was only modestly effective in treatment-naïve tumors (fig. S11, D and E). Together, these results mirror those from the BKM120 trials and

suggest that continued CSF-1R inhibition is necessary to drive IGF1R/PI3K signaling dependency, rendering recurrent tumors sensitive to pathway inhibition. Similar combination treatment efficacy and mechanistic commonalities (including IF quantification of Ki67:CC3 ratios, CD206, and p-IGF-1R) were observed in orthotopic xenograft trials performed with patient-derived proneural tumorspheres and with established human glioma cell lines (Fig. 7, E and F, and fig. S12, A to F).

To determine whether tumor outgrowth could be prevented by earlier IGF-1R inhibition, PDG mice with high-grade GBMs were treated continuously with BLZ945 alone until 28 days, at which point OSI906 was added until the trial endpoint (Fig. 7A, trial design 2). With early combination treatment, we indeed extended overall survival and increased the percentage of animals that survived to endpoint (89% BLZ945 + OSI906 versus 44% BLZ945 alone or 0% OSI906 alone) (Fig. 7G). Together, our results suggest that targeting either IGF-1R or PI3K signaling in GBMs resistant to CSF-1R inhibition may interfere with disease progression and improve overall survival.

Given that pharmacological inhibition of IGF-1R using OSI906 cannot confirm whether tumor cell-specific blockade is sufficient to reduce recurrent disease, we used a genetic approach to target this receptor in glioma cells. U251 glioma cell lines were genetically engineered to express a doxycycline (dox)-inducible short hairpin RNA (shRNA) against *IGF1R*, and orthotopic xenograft experiments were performed (trial design is provided in fig. S13A). Two independent shRNAs targeting *IGF1R* were used, and a scramble-sequence shRNA was used as a control (fig. S13, B to D). We found that in both cases, dox-induction of the shRNAs during the rebound phase of the trial (day 12) mitigated tumor progression compared with no-dox control animals (Fig.

7H and fig. S13E). These results support our hypothesis that tumor cell-specific IGF-1R contributes to BLZ945 resistance and disease recurrence.

Discussion

Here, we describe the development of acquired resistance to CSF-1R inhibition in mouse models of GBM. Although initial therapeutic response to CSF-1R inhibition is robust, rapid, and completely penetrant, we found that approximately half of the animals eventually develop resistance, with rapidly progressing rebound tumors. In light of recent results from ongoing patient studies with CSF-1R inhibitors in glioma (46) and other cancers, our findings suggest the need to prepare for the emergence of therapeutic resistance to CSF-1R inhibitors in GBM in the clinical setting and determine whether brain malignancies other than GBM will respond similarly to CSF-1R inhibition. Although classical mechanisms of tumor cell-intrinsic resistance to cytotoxic and targeted agents have been well-defined—including aberrant drug metabolism and transport, drug target mutation, and activation of alternative survival pathways (47)—it still remains unclear whether resistance to TME-directed therapies will follow similar principles. Given that TME-targeted agents are increasingly being evaluated in the clinic (1, 2), it will be critical to mechanistically define how resistance evolves in response to these therapies in order to provide long-term disease management for patients.

In light of this problem, we have now identified a mechanism of drug resistance that can circumvent therapeutic response to a TME-targeted therapy and promote disease progression in the absence of tumor cell-intrinsic alterations. Specifically, we have uncovered a heterotypic paracrine signaling interaction that is initiated by the TME and drives resistance to CSF-1R inhibition. In rebound tumors, we found that IGF-1 is up-

regulated in TAMs in response to IL4 (possibly supplied by T cells or alternative cell types), in part via NFAT activation. IGF-1 secretion into the extracellular environment results in activation of IGF-1R and PI3K signaling in glioma cells, supporting tumor growth and malignancy (Fig. 8, model). Multiple nodes in this signaling loop can be targeted therapeutically by agents that are currently used clinically—including OSI906, BKM120, or FK506—resulting in a substantial improvement in survival in the preclinical setting when combined with CSF-1R inhibition. Indeed, given that PI3K signaling is aberrantly activated in a substantial proportion of GBM patients (16), and that recent clinical trial results show limited efficacy

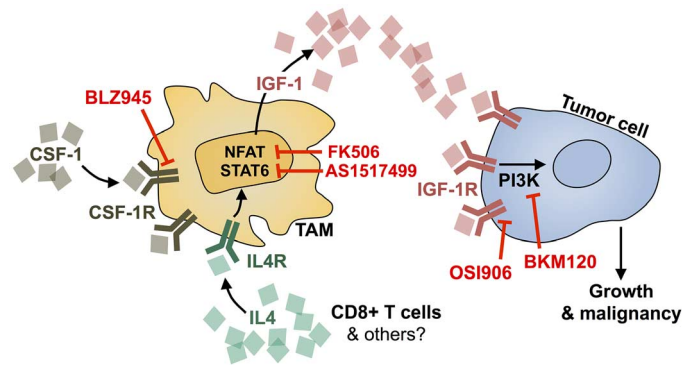


Fig. 8. Working model for mechanism of resistance to CSF-1R inhibition in glioma.

IGF-1 is up-regulated in TAMs in response to long-term CSF-1R inhibition in GBM. IGF-1 secretion into the extracellular environment results in activation of IGF-1R on tumor cells and downstream PI3K signaling to support tumor regrowth during continuous BLZ945 treatment. Upstream of IGF-1 in TAMs, NFAT and/or Stat6 transcriptional activity regulate its expression. This is thought to be initiated in response to IL4/IL4R pathway activation, feeding in from other cell types in the TME, including T cells (and possibly others). Multiple nodes in this signaling loop can be targeted therapeutically—including OSI906, BKM120, AS1517499, or FK506—resulting in a substantial improvement in survival in preclinical trials when combined with CSF-1R inhibition.

in recurrent (albeit very advanced) GBM (46), it is possible that this pathway could similarly contribute to intrinsic resistance to CSF-1R inhibition, and consequently, those patients may benefit from combinatorial inhibition of these pathways from the outset.

Our findings underscore the importance of bidirectional feedback between cancer cells and their microenvironment and support the notion that although stromal cells are less susceptible to genetic mutation than are cancer cells, a tumor can nonetheless persist by exploiting its extracellular environment to acquire a resistant phenotype. Thus, we propose that an integrated analysis of cancer cells with their microenvironment will be critical to understanding both their parallel evolution during tumor progression and their capacity for adaptation in the context of therapeutic intervention and the development of resistance.

Materials and methods

Study design

The overall objective of our study was to understand how resistance to CSF-1R inhibitors develops in high-grade glioma by using various *in vivo* and *in vitro* models. Within the animal studies, mice were randomly assigned to different therapy groups, which included treatment with BLZ945 (a CSF-1R inhibitor) in combination with inhibitors of putative resistance pathways (such as IGF-1R or PI3K), versus single-agent or vehicle controls. Survival and disease progression were monitored by using a combination of MRI, histology, flow cytometry, and gene expression analyses throughout all trials. To power our studies, sample size was predefined as at least $n = 3$ independent experiments, replicates, or samples for *in vitro* and *in vivo* experiments, and up to a maximum of $n = 90$ mice for survival analyses. Replicate values are indicated for each experiment in corresponding figure legends. All analyses were calculated in a blinded manner through numerical coding of samples. For all long-term survival trials, 26 weeks was selected as a predefined endpoint because mice in the *Ink4a/Arf*^{-/-} background develop spontaneous lymphomas and sarcomas beginning at ~30 weeks of age. For *in vivo* trials, mice were considered outliers if they developed (i) spontaneous lymphomas (given this disposition in the *Ink4a/Arf*^{-/-} background), (ii) early symptoms of tumor burden >1 week before trial enrollment, or (iii) development of hydrocephalus before trial enrollment.

Biologicals and pharmaceuticals

BLZ945 (8) was obtained from Novartis (Basel, Switzerland) for both *in vitro* and *in vivo* use; 6700 nM BLZ945 was used for all *in vitro* experiments in tumor cells, versus an equal percent dimethyl sulfoxide (DMSO) as a vehicle control. This concentration represents 100 times the median inhibitory concentration (IC₅₀) for BLZ945 in macrophages (8). For *in vivo* experiments, BLZ945 was obtained preformulated at 12.5 mg/ml. BLZ945 was administered orally 1× daily at 200 mg/kg, and 20% Captisol was used as a vehicle control. BKM120

(Buparlisib; 1 μM unless indicated otherwise), AEW541, ADW742, BMS754807, and OSI906 (Linsitinib; 10 μM unless indicated otherwise) were purchased from Selleckchem (Houston, TX) for *in vitro* use and were used up to 100 μM for dose response assays versus an equal percent DMSO as a vehicle control. BKM120 and OSI906 were purchased from ChemieTek (Indianapolis, IN) for *in vivo* use. BKM120 was formulated by dissolving 52 mg into 500 ml NMP, boiling, and then adding 9.5 ml of PEG300. BKM120 was administered orally 1× daily at 20 mg/kg, and NMP:PEG300 (1:19) was used as a vehicle control. Animals were dosed at 20 mg/kg so as to avoid off-target effects, because BKM120 binds tubulin at concentrations above 50 mg/kg in subcutaneous tumor models, but not below 40 mg/kg (15). OSI906 was formulated daily at 4 mg/ml in 25 mM tartaric acid with shaking and sonication for ~15 min. OSI906 was administered orally once daily at 40 mg/kg, and 25 mM tartaric acid was used as a vehicle control. We chose to treat at 40 mg/kg because the maximum tolerated dose for OSI906, 75 mg/kg (48), was found to be toxic within 4 days in our studies. For all combination trials, BLZ945 was administered in the morning, and BKM120 or OSI906 was administered in the evening. The NFAT inhibitor, INCA-6, was purchased from Tocris (Bristol, UK) and was used at a concentration of 40 μM for *in vitro* use (49). For *in vivo* inhibition of NFAT signaling, FK506 was used to inhibit the activating interaction between calcineurin and NFAT, at a dose of 10 mg/kg (administered intraperitoneally every 3 days) (50). The Stat6 inhibitor, AS1517499, was purchased from Axon Medchem (Reston, VA) and was used at a concentration of 50 nM for *in vitro* use and dosed at 10 mg/kg for *in vivo* use (administered intraperitoneally 2× weekly) (51). The vehicle control for FK506 and AS1517499 *in vivo* was 10% ethanol (EtOH) and 1% Tween-80 in phosphate-buffered saline (PBS). For *in vitro* PCR assays, recombinant mouse IL4 (R&D Systems, Minneapolis, MN) was used at a concentration of 10 ng/ml, recombinant mouse TGFβ1 (R&D Systems) was used at a concentration of 50 ng/ml, and the TGFβ1 type 1 receptor inhibitor SB431542 (Tocris) was used at a concentration of 10 μM. For *ex vivo* GMEC assays, a neutralization antibody against IGF-1 (R&D Systems) was used at a concentration of 0.5 μg/ml. For culture of macrophages *in vitro*, recombinant mouse CSF-1 was used at a concentration of 10 ng/ml. For *in vitro* assays using BMDMs, CSF-1 supplementation was excluded from all experimental conditions.

Animals

Cr1:NU(NCr)-Foxn1^{tmu} immunodeficient mice were purchased from Charles River Laboratories (Wilmington, MA) for orthotopic transplantation studies. NOD/CB17-Prkdc^{scid} immunodeficient mice were purchased from The Jackson Laboratory (Bar Harbor, ME) for orthotopic implantation of human cells. Three different transgenic mouse models expressing the avian tv-a receptor under the control of the nestin (N) promoter in either mixed strain or BL6 backgrounds were used (Ntv-a;*Ink4a/Arf*^{-/-},

Ntv-a, and Ntv-a;*Pten*^{flax}), all previously described (13, 52–57) and bred within the MSKCC animal facility. *Stat6*^{-/-}, *Il4rd*^{flax}, *LysM-cre*, and WT C57BL/6 (BL6) mice were also bred within the MSKCC animal facility and were used for bone marrow isolations. All animal studies were approved by the Institutional Animal Care and Use Committee of MSKCC.

PDG mouse model

The initiation of PDGF-driven gliomas (PDGs) with RCAS-hPDGF-B-HA in adult mice has been previously described (8, 13, 58). Briefly, Ntv-a;*Ink4a/Arf*^{-/-} mice were fully anesthetized with ketamine/xylazine before surgery. Pain management included a 50-μl subcutaneous injection of bupivacaine (0.25%) at the surgical site before surgery, and an intraperitoneal injection of buprenorphine immediately after surgery. Mice were intracranially injected with DF-1:RCAS-hPDGF-B-HA cells (200,000 cells/1 μl) between 5 and 6 weeks of age by using a fixed stereotactic apparatus (Stoelting, Wood Dale, IL). Injections were made into the right frontal cortex, ~1.5 mm lateral and 1 mm caudal from bregma, and at a depth of 2 mm into the subventricular zone (SVZ). In this model, injection into the SVZ induces tumors with low latency (4 to 5 weeks), 100% penetrance, and histological features characteristic of patient GBM including microvascular proliferation and pseudopalisading necrosis (13). The incision was sealed by using Vetbond tissue adhesive (3M, Maplewood, MN). Tumors were imaged with MRI after 5 weeks, and drug intervention was initiated for tumors ≥2 mm³. A total of 90 animals were treated in long-term experiments with BLZ945 alone, which represented five independent cohorts. These data are compiled and presented in Figs. 1D, 2E, and 7G (red lines).

p53 KD mouse model

Injections were performed as described for the PDG mouse model above, except Ntv-a mice were used (WT *Ink4a/Arf*). Mice were intracranially injected with a 1:1 ratio of DF-1:RCAS-hPDGF-B-HA cells and DF-1:RCAS-shp53 cells (total of 300,000 cells/2 μl) between 5 and 6 weeks of age. Injection into the SVZ in the p53 knockdown (KD) model induces high-grade tumors with low latency (6 to 7 weeks), 100% penetrance, and histological features of human GBM (13, 54, 55). Tumors were detected by MRI after 6 to 7 weeks, at which point drug intervention with BLZ945 was initiated (Fig. 2F).

Pten KO mouse model

Injections were performed as described for the PDG mouse model above, except Ntv-a;*Pten*^{flax} mice were used (WT *Ink4a/Arf*). Mice were intracranially injected with a 1:1 ratio of DF-1:RCAS-hPDGF-B-HA cells and DF-1:RCAS-Cre cells (total of 300,000 cells/2 μl) between 5 and 6 weeks of age. Injection into the SVZ in the *Pten* KO model induces tumors with moderate latency (8 to 12 weeks) and penetrance (~20 to 30%). Tumors that form harbor key characteristics of human GBM, including highly infiltrative histology (13, 54, 56, 57). Tumors were detected with

MRI after 8 to 12 weeks, at which point drug intervention with BLZ945 was initiated (Fig. 2, F and G).

Derivation of mouse primary glioma cell lines from PDG tumors

To derive rebound or dormant cell lines from BLZ945-treated PDG tumors, MRI was used to confirm whether a particular tumor was in rebound or dormancy phase. Macrodissected rebound or dormant lesions from the BLZ945-treated PDG mouse model were manually dissociated and filtered through a 40- μ m-mesh filter. The cell suspension was washed twice with PBS and cultured in Mouse Neural Stem Cell (mNSC) Basal Media (Stem Cell Technologies, Vancouver, Canada) containing mNSC proliferation supplement, 1 mg/ml Heparin (Stem Cell Technologies), 10 ng/ml recombinant epidermal growth factor (rEGF; Invitrogen, Carlsbad, CA), and 20 ng/ml recombinant basic-fibroblast growth factor (rbFGF; Sigma, Bandai, Japan). To generate cell lines in monolayer, tumorsphere cultures were expanded, dissociated, and transferred to culture with Dulbecco's minimum essential medium (DMEM) + 10% fetal bovine serum (FBS) (59). In total, five rebound cell lines were derived (89AReb, 89BREb, 74Reb, 48Reb, and 52Reb), and one cell line was derived from the 28-day dormant time point. The 28-day dormant cells (fig. S8G) took several weeks before starting to proliferate in culture, and upon transplantation into naïve animals, the cells did not give rise to growing tumors [bioluminescent imaging (BLI) signal remained stable and was monitored up to 22 days]. Derivation of the PDGC23 primary glioma cell line from an untreated/naïve mixed-background PDG mouse was described previously (8).

Human cell lines

Human umbilical vein endothelial cells (HUVECs) were purchased from ATCC (Manassass, VA). Human brain microvascular endothelial cells (HBMECs) and human astrocytes were purchased from Sciencell (Carlsbad, CA). Astrocytes were cultured on poly-L-lysine-coated plates, and both HUVECs and HBMECs were cultured on gelatin-coated plates with endothelial cell media (ECM; Sciencell) + 10% FBS + an endothelial cell growth factor supplement. The U251 (commercially available) and TS573 (patient-derived) cell lines were selected on the basis of our previously published work, which showed efficacy in response to BLZ945 in orthotopic xenograft trials (8). The patient-derived TS573 glioma tumorsphere line was derived from a consenting patient under Institutional Review Board (IRB)-approved protocols for the banking of excess tumor tissue during routine surgical resection [MSKCC IRB nos. 99-125A(2) and 06-107], as previously described (8, 60). Tumorspheres were maintained in Human Neural Stem Cell (hNSC) Basal Media (Stem Cell Technologies) containing hNSC proliferation supplement, 1 mg/ml Heparin (Stem Cell Technologies), 10 ng/ml rEGF (Invitrogen), and 20 ng/ml rbFGF (Sigma). Tumorspheres were passaged by dissociation with Accutase cell detachment solution (Millipore,

Billerica, MA). Characterization and molecular subtyping by Sequenom (San Diego, CA) and NanoString (Seattle, WA) and aCGH were performed as previously described (8). Briefly, aCGH on primary spheroids showed a high-level amplification of *PDGFRA* and *CDK6* loci and a regional chromosome 5 loss. NanoString analysis confirmed *PDGFRA* overexpression, and Sequenom analyses were negative for *IDH1/2* mutations.

Isolation of BMDMs

To generate macrophages from bone marrow, femurs and tibiae from *Stat6*^{-/-}, *Il4ra*^{fllox}; *LysM-cre*, or WT BL6 mice were flushed and cells harvested under sterile conditions. The isolate was filtered through a 40- μ m-mesh filter and cultured in 30-ml Teflon bags (PermaLife PL-30) for 5 to 7 days in DMEM + 10% FBS + 10 ng/ml recombinant mouse CSF-1 (R&D Systems). Media were changed every other day.

TGL infections

Cell lines were labeled with a triple-imaging vector [TK-GFP-Luc (TGL)] (61) for use in orthotopic in vivo experiments. The TGL vector was developed to enable noninvasive in vivo imaging of tumor growth over time. A standard protocol for retroviral infection was used. Briefly, GP2-293T cells were transfected with the TGL construct and pCL-Ampho at a 1:1 ratio, using Fugene (Promega, Madison, WI) and OptiMEM (Gibco, Thermo Fisher). Twelve hours later, media was replaced with complete antibiotic-free DMEM and collected for 3 consecutive days for infection of target cells.

Orthotopic transplantation experiments

TGL-labeled cells were resuspended in antibiotic-free, serum-free DMEM for all orthotopic injections. Mice were fully anesthetized with ketamine/xylazine before surgery. Pain management included a 50- μ l subcutaneous injection of bupivacaine (0.25%) at the surgical site before surgery, and an intraperitoneal injection of buprenorphine immediately after surgery. Mice were intracranially injected with glioma cells between 5 and 6 weeks of age by using a fixed stereotactic apparatus (Stoelting). The number of cells injected was as follows: mouse glioma lines, 2.5×10^4 to 5×10^4 cells/2 μ l; human U251 cells, 2.5×10^5 cells/2 μ l; and patient-derived TS573 cells, 5×10^4 cells/2 μ l. Injections were made to the right frontal cortex, ~1.5 mm lateral and 1 mm caudal from bregma and at a depth of 2 mm. Hydrogen peroxide was used to clean the hole made by the surgical drill, and bone wax was used to close the hole. The incision was sealed by using Vetbond tissue adhesive (3M). One week after injections, mice were randomly assigned to vehicle or BLZ945 treatment groups and dosed 1 \times daily by means of oral gavage. BLI (Xenogen IVIS-200 Optical In Vivo Imaging System) was performed every 3 to 5 days over the course of the experiment in order to monitor tumor progression and response to therapy. Once BLZ945-treated tumors reached three times the volume of their lowest BLI measurement, tumors were considered "resistant," and mice were randomly assigned to combination

treatment with BLZ945 + OSI906, or BLZ945 + vehicle. For dox-inducible *IGF1R* shRNA experiments with U251 cells, mice were additionally assigned to either \pm dox groups (dox hyclate diet formulated at 2500 mg/kg; Envigo, Cambridge-shire, UK).

Animal sacrifice and tissue harvest

Mice were euthanized at the defined 26-week endpoint, or when symptomatic (poor grooming, lethargy, weight loss, hunching, macrocephaly/hydrocephalus, or seizures). We selected 26 weeks because mice in the *Ink4a/Arf*^{-/-} background develop spontaneous lymphomas and sarcomas beginning at ~30 weeks of age (62). Euthanasia was performed by means of either carbon dioxide asphyxiation or anesthesia (avertin; 2,2,2-tribromoethanol; Sigma) followed by cervical dislocation. For snap freezing of whole-tumor samples, mice were euthanized 1 hour after the last treatment dose, and tissues were collected, frozen immediately in liquid nitrogen, and stored at -80°C for subsequent applications (such as RNA isolation and protein extraction). For isolation of whole tissues for histology, mice were fully anesthetized with avertin, transcardially perfused with 10 ml of PBS, followed by 10 ml of paraformaldehyde (PFA; 4% in PBS). Tissues were incubated in PFA overnight at 4°C, rinsed in PBS, and then transferred to sucrose (30%) for 2 to 3 days at 4°C. For hypoxia analysis, mice were injected intraperitoneally with 60 mg/kg of pimonidazole [hypoxyprobe-1 (HPI)] ~20 min before sacrifice and tissue collection. All tissues were embedded and frozen in Optimal Cutting Temperature (OCT) compound (Tissue-Tek), and 10- μ m cryostat tissue sections were used for all subsequent staining and analyses.

IF staining

For IF staining, 10- μ m frozen sections were thawed and dried at room temperature and rinsed in PBS. Tissue sections were blocked in 0.5% Blocking Reagent (PerkinElmer, Boston, MA) (1 hour at room temperature or overnight at 4°C), followed by incubation in primary antibody (2 hours at room temperature or overnight at 4°C). All primary antibodies and dilution factors are listed in table S4. Sections were then washed in PBS and incubated with the appropriate fluorophore-conjugated secondary antibody (Molecular Probes, Eugene, OR) at a dilution of 1:500 in 0.5% PNB (1 hour at room temperature). 4',6-diamidino-2-phenylindole (DAPI) was used as a counterstain before mounting with fluorescent mounting media (Dako, Carpinteria, CA).

IHC and Von Kossa staining

For manual IHC, tissue sections were first subjected to citrate buffer-based antigen retrieval by submerging in antigen unmasking solution (0.94% v/v in distilled water; Vector Laboratories, Burlingame, CA) and microwaving for 10 min, followed by cooling to room temperature for \geq 30 min. Endogenous peroxidases were blocked for 10 min with Dual Endogenous Enzyme Block (Dako). Slides were incubated with serum-free protein block (Dako) for 1 hour at room temperature

and then incubated with primary antibody in a humidity chamber overnight at 4°C. The following day, slides were washed and incubated with horseradish peroxidase (HRP)-conjugated secondary antibodies (Jackson Immunoresearch, West Grove, PA) for 1 hour at room temperature, and positive staining was detected by using diaminobenzidine (DAB) substrate-chromogen. Haematoxylin was used as a counterstain, and slides were mounted with VECTASHIELD mounting media (Vector Laboratories). As an alternative to manual staining, a Ventana autostainer was used for staining of mouse glial fibrillary acidic protein (GFAP), human phospho (p)-AKT, and human MRC1, which included automated deparaffinization, citrate buffer-based antigen retrieval, non-specific protein and endogenous peroxidase block, antibody incubation, and DAB detection. All primary antibodies and dilution ratios for both manual staining and autostaining are listed in table S4. For visualization of calcium deposition in tissue sections, a Von Kossa staining kit was used as per manufacturer's instructions (Abcam, Cambridge, UK). Briefly, tissues are treated with a silver nitrate solution, which is deposited by replacing calcium reduced by ultraviolet light. Nuclear fast red was used as a counterstain (Vector Laboratories).

Histology and grading

For analysis of tissue histology and grading of tumor malignancy, hematoxylin and eosin (H&E) staining was performed by using a Tissue-Tek automated slide stainer, and slides were mounted with VECTASHIELD mounting media (Vector). Tissues were blindly graded by a neuropathologist (J. Huse, MSKCC) according to standard World Health Organization criteria (63). For central nervous system tumors, this grading system is based on a malignancy scale, in which tumors that are minimally proliferative and infiltrative are considered grade I, whereas the most histologically aggressive, infiltrative, and incurable tumors (glioblastomas) are grade IV (63). GFAP quantification was performed by use of the Allred scoring method, which is the sum of a proportion score (0 to 5) and an intensity score (0 to 3) for a given marker (64).

Image analysis

Stained tissue sections were visualized under a Carl Zeiss (Oberkochen, Germany) Axioimager Z1 microscope equipped with an ApoTome.2, or a Carl Zeiss Axioimager M1 epifluorescence and brightfield microscope. Staining analyses were performed by using a TissueGnostics (Vienna, Austria) slide scanning platform and TissueQuest analysis software. This automated analysis platform was used to quantify number of positive counts, area of positive staining, and/or microvascular density within stained tissue sections in an unbiased manner (8).

Patient GBM tissue samples

Patient GBM tissue samples used for staining and analysis (Fig. 5I and fig. S9B) were obtained from the Brain Tumor Center, MSKCC. Eighteen

patient tissue samples were used in total. IHC staining for MRC1 and p-AKT was performed as described above ("IHC and Von Kossa staining," above), and quantitation was performed by using the Axioimager Z1 scanning microscope ("Image analysis," above). Correlational analysis across patients was performed by using GraphPad Prism 6.0 ("Data presentation and statistical analysis," below). Patient information for all samples can be found in table S2.

Protein isolation and immunoblotting

To evaluate phospho-protein status of IGF-1R and AKT in culture, cells were seeded at 70 to 80% confluence, serum-starved for ~12 hours, and then treated with OSI906 for 30 min. To evaluate phosphorylation of IGF-1R or AKT in snap-frozen tumor samples, tissues were dissociated with a glass homogenizer on ice in the presence of lysis buffer. All protein lysates were prepared in radio-immunoprecipitation assay lysis buffer supplemented with Halt protease inhibitor (1:100; Thermo Scientific, Waltham, MA) and Halt phosphatase inhibitor (1:100; Thermo Scientific), and protein was quantified by using a BCA protein assay kit (Pierce). Equal amounts of protein (20 µg/lane for cell lines, and 100 µg/lane for tissue samples) were loaded onto SDS-polyacrylamide gel electrophoresis precast gels (Invitrogen) and transferred to polyvinylidene difluoride membranes for immunoblotting. Membranes were blocked in 5% milk, incubated with primary antibodies (table S4) for 1 hour at room temperature or overnight at 4°C, washed with 0.1% Tris-buffered saline and Tween 20 (TBS-T), and incubated with HRP-conjugated secondary antibodies (Jackson Immunoresearch) for 1 hour at room temperature. SuperSignal West Femto or Pico chemiluminescent substrate and CL-XPosure Film (Pierce) were used for signal detection.

RNA isolation, reverse transcription, and quantitative RT-PCR

RNA was isolated with TRIzol and deoxyribonuclease-treated, and 1 µg of RNA was used for cDNA synthesis by using a High Capacity cDNA Reverse Transcription kit (Applied Biosystems, Foster City, CA). Mouse taqman probes (Applied Biosystems) were used for quantifying expression of *Igf1* (Mm00439560_m1), *Chil3* (Mm00657889_mH), *Ccl17* (Mm01244826_g1), *Retnla* (Mm00445109_m1), *Il4* (Mm00445260_m1), *Arg1* (Mm00475988_m1), *Cd36* (Mm00432403_m1), *Mrc1* (Mm01329362_m1), *Ubc* (Mm02525934_g1; housekeeping), and *Hprt* (Mm01545339_m1; housekeeping). Human taqman probes (Applied Biosystems) were used for quantifying expression of *IL4* (Hs00174122_m1), *IL13* (Hs00174379_m1), *IGF1* (Hs01547656_m1), and *HPRT1* (Hs02800695_m1; housekeeping).

MTT assays

Cell growth rate was determined by using a MTT cell proliferation kit (Roche, Basel, Switzerland). Briefly, cells were plated in ≥triplicate in 96-well plates; 1×10^3 cells/well were plated for mouse glioma cell lines, and 5×10^3 cells/well were plated for BMDMs. For BLZ945 time course ex-

periments, cells were grown in the presence of 6700 nM of BLZ945 versus an equal percent DMSO, media was changed every 48 hours, and viability measurements were taken every 24 hours. For dose response experiments, cells were grown in the presence of an IGF-1R inhibitor (AEW541, ADW742, BMS754807, or OSI906) versus an equal percent DMSO at the doses indicated ("Biologicals and pharmaceuticals," above), and viability measurements were taken after 24 hours. Reduction of the MTT substrate was detected with colorimetric analysis by using a plate reader as per the manufacturer's protocol. Ten microliters of MTT labeling reagent was added to each well and then incubated for 4 hours at 37°C, followed by the addition of 100 µl of MTT solubilization reagent overnight. The mixture was gently resuspended, and absorbance was measured at 595 and 750 nm on a spectraMax 340pc plate reader (Molecular Devices, Sunnyvale, CA).

Ex vivo GMEC assays

GMECs are early-passage heterotypic cell cultures harvested directly from PDG mouse primary tumors. Flow cytometry characterization of these cultures revealed that passage 1 GMECs contain a high abundance of tumor cells, astrocytes, and macrophages, as well as smaller proportions of myeloid progenitors, T cells, and B cells (fig. S8I). In our ex vivo assays, we derived CM from passage 1 rebound GMECs and used this CM to treat naïve BMDMs in vitro (experimental design is provided in fig. S8J). We collected CM from these GMEC-stimulated BMDMs (Stim CM) and applied it to either rebound glioma cell lines (highly sensitive to IGF-1R inhibition) or naïve glioma cell lines (less sensitive to IGF-1R inhibition), plus or minus a neutralizing antibody for IGF-1. An MTT assay was used to assess changes in growth in response to each treatment condition, as described above.

Flow cytometry and FACS on primary mouse tissues

Mice were fully anesthetized with avertin and transcardially perfused with 20 ml of PBS. The brain was then isolated, and the tumor was macrodissected from the surrounding normal tissue. Tissues were mechanically dissociated and filtered into a single-cell suspension. For flow cytometry, cells were counted and incubated with Fc block for 1 hour (1:100/10⁶ cells; BD Biosciences, East Rutherford, NJ), followed by a 30-min incubation with LIVE/DEAD fixable dead cell kit (Invitrogen) and then a 1-hour incubation with conjugated antibodies for extracellular markers. For FACS, cells were counted and incubated with Fc block for 1 hour, followed by a 1-hour incubation with conjugated antibodies, and then stained with DAPI for dead-cell exclusion. All antibodies and dilution ratios used for these experiments are listed in table S4. OneComp eBeads (eBioscience, San Diego, CA), ArC Amine Reactive Compensation Beads (Invitrogen), and/or cell suspensions from spleen were used for compensation controls. A BD Biosciences LSR-Fortessa was used for flow cytometry, and a

BD Biosciences FACS Aria III was used for cell sorting.

Distinguishing between putative BMDMs and microglia by flow cytometry

Flow cytometry was used to evaluate the proportions of peripherally derived BMDMs versus resident microglia in PDG tumors across different treatment groups, according to published methods (22–24). Briefly, after gating on live cells we used cell-surface expression of CD45 and CD11b to distinguish between the two populations, in which CD45^{lo} CD11b⁺ defined putative microglia, whereas CD45^{hi} CD11b⁺ defined putative BMDMs. In using this method, we acknowledge its limitations and recognize that these two populations cannot be definitively distinguished without lineage-tracing experiments that specifically label yolk sac-derived microglia or peripherally recruited BMDMs.

FACS purification of human peripheral immune cell types

Human buffy coats from three consenting healthy donors were obtained from the New York Blood Center. For isolation of neutrophils and eosinophils, buffy coats were directly red blood cell lysed (BD Biosciences PharmLyse) for 15 min at room temperature. All other cell types were isolated from the top layer of a Ficoll gradient separation (HistoPaque, Sigma). Cells were pelleted for 10 min at 300g and washed twice with FACS buffer (PBS + 2% fetal bovine serum) and Fc blocked (Biolegend TruStain FcX). Cells were incubated with the appropriate antibodies for 15 min (table S4). Cells were FACS-purified on an Aria III (BD Biosciences). For human macrophage differentiation, PBMCs were isolated from buffy coats following a Ficoll gradient. Monocytes were further purified from the interphase of a 70/30% Percoll gradient. Monocytes were then washed twice with PBS and cultured in Teflon bags (Origin) for 7 days in DMEM + 2% human serum + recombinant human CSF-1 (10 ng/ml; R&D Systems). CSF-1 and media were replaced every 48 hours.

aCGH

All sequencing and quality control was performed at the Integrated Genomics Operation, MSKCC. DNA was isolated from passage 1 PDG neurospheres from rebound tumors or corresponding liver tissue by using TRIzol as per manufacturer instructions (Invitrogen). Three micrograms of DNA was used with an Agilent (Santa Clara, CA) standard cy5/cy3 labeling protocol. Briefly, Agilent Mouse CGH 180k arrays were hybridized at 65°C and 20 revolutions per min for 40 hours. Slides were then scanned by using the Agilent scanner according to the manufacturer's instructions. The raw data were extracted with Feature Extraction by using Agilent default analysis settings. Subsequent analyses were performed in R v3.1.0 by using the "DNAcopy" package (65).

RNA-seq

Three RNA-seq experiments were performed in total: (i) FACS-purified tumor cells (CD45⁺PDGFR α ⁺)

and TAMs (CD45⁺CD11b⁺Gr1⁺) from Veh, EP, and Reb tumors; (ii) FACS-purified astrocytes (CD45⁺GLAST⁺), B cells (CD45⁺CD19⁺), Tc cells (CD45⁺CD3⁺CD8⁺), and bulk T cells (CD45⁺CD3⁺CD8⁻) from Reb tumors; and (iii) FACS-purified TAMs (CD45⁺CD11b⁺Gr1⁺) from 28-day and Reb tumors. RNA-sequencing and quality control was performed at the Integrated Genomics Operation, MSKCC, or Genewiz (Plainfield, NJ). In all cases, RNA was isolated by using TRIzol as per manufacturer instructions (Invitrogen), and RNA integrity was assessed with an Agilent Bioanalyzer 2100. RNA-seq libraries were prepared by using the SMART-Seq library preparation kit, and 2 × 50 or 2 × 100 base pair sequencing was performed on an Illumina HiSeq.2000. Sequencing quality was assessed with FASTQC (www.bioinformatics.babraham.ac.uk/projects/fastqc). Reads were mapped to the mouse genome (mm10) by using STAR 2.3.0e (66) with the default parameters, a minimum intron length of 70 base pairs, and a maximum of 100,000 base pairs. BAM files were generated and sorted, and duplicate reads were then removed by using SAMTOOLS (67). Read counts were tabulated with HT-Seq by using "union" mode and the iGenomes GFF file as a reference (Illumina) (68).

Gene expression analyses

Raw count data from HT-Seq was imported into R (v3.1.0) and normalized by using limma voom (69). Principal component analysis was completed by using the princomp function on mean centered data. A log₂-fold change cutoff of 1 and a false discovery rate of 10% were applied for all differential gene expression analyses (table S1). Significantly up-regulated genes from these lists were used in gene ontology analyses by using DAVID (70). GSVA was performed on RNA-seq data from FACS-purified PDGFR α ⁺ tumor cells, using the GSVA package (14) with gene sets from the C2 group from the Molecular Signatures Database (MSigDB) (71). A log₂-fold change cutoff of 1 and a false discovery rate cutoff of 10% were used to determine differentially enriched gene sets (fig. S3B). The spectrum model of macrophage activation was assessed with GSEA, using the gsea function from the phenotest package in R (<http://rpackages.ianhowson.com/bioc/phenotest>). A minimum *P* value of <1 × 10⁻¹⁶ was used to represent significance values that were reported as 0.0 and outside of the determined distribution. Gene sets were adapted from a previous study in which mouse macrophages were stimulated with IFN- γ , IL-4, TNF- α , TGF- β , IL-1 β , MALP2, or CPG (27). A literature-derived IL-4 responsive gene set was generated through the use of QIAGEN's Ingenuity iReport (www.qiagen.com/ingenuity).

TF activity analysis

TF activity analysis was performed as an adaptation of previously published methods: ISMARA (72) and RegulatorInference (73). Briefly, transcription start sites and Motevo predictions (74) of binding sites were downloaded from the SwissRegulon (<http://swissregulon.unibas.ch/>)

(fegi.sr/downloads). These were used to determine the number of predicted binding sites for 185 TF families across all mouse promoters. Promoters were designated as 2 kb upstream and downstream of transcription start sites. This tabulated matrix was then used in a ridge regression to model log₂ gene expression values generated by means of voom. Ridge regression was performed with the glmnet function in R (75). The regularization parameter, λ , was identified for each sample through 10-fold cross validation. The coefficients for each TF family were *z*-scored and used as relative TF activity scores in subsequent analyses. Differentially enriched TFs were identified by using the *z*-scored values in limma with a log₂-fold change cutoff of 1 and a false discovery rate of 10% (table S3).

External data set analysis

RNA-seq expression data from the TCGA glioblastoma patient data set was downloaded by using TCGA-assembler (76). For survival analyses, these data were filtered for patients with updated clinical information from the Broad Firehose. Correlations between *IGF1* and macrophage markers (*CD163*, *MRC1*, *CSF1R*, *CD68*, and *AIF1*) or astrocyte markers (*GFAP* and *ALDH1L1*) were assessed by using a Spearman correlation coefficient. Normalized gene expression data for human bulk tumor versus tumor-associated macrophage fraction were downloaded from the Gene Expression Omnibus (GEO) under accession no. GSE16119 (44). Subtype calls for patients were obtained from GlioVis (<http://gliovis.bioinfo.cnio.es>). *PI3K* signature scores were tabulated with a single-sample gene set enrichment, as used for macrophage activity analysis. The gene set was from the Hallmark collection from MsigDB, systematic name M5923 (43).

Data availability

All sequencing data has been deposited to the GEO under the accession no. GSE69104 and aCGH data under the accession no. GSE80399. All code used in this project can be found at <https://bitbucket.org/bowmanr/joycelab-brain-tme>.

Data presentation and statistical analysis

GraphPad Prism 6.0 or R Studio was used for all data analysis. Parametric data are presented as mean \pm standard error (SEM) and were analyzed by means of an unpaired two-tailed Student's *t* test. For multiple comparisons, a one-way analysis of variance (ANOVA) with Tukey's or Dennett's correction was used as noted in the figure legends. Nonparametric data were analyzed by means of a Mann-Whitney test on ranks. For survival curves, *P* values were obtained by using the Log Rank (Mantel-Cox) test. Fisher's exact test was used for histological tumor grading. A pairwise Spearman correlation test was used for correlational analyses. *P* < 0.05 was considered as statistically significant in all cases. Principal component analyses, correlation plots, Volcano plots, heatmaps, and network plots were plotted in R Studio using

base graphics (www.R-project.org), rgl (<http://CRAN.R-project.org/package=rgl>), gplots (<http://CRAN.R-project.org/package=gplots>), ggplot2 (77), and qgraph packages (78).

REFERENCES AND NOTES

- D. F. Quail, J. A. Joyce, Microenvironmental regulation of tumor progression and metastasis. *Nat. Med.* **19**, 1423–1437 (2013). doi: [10.1038/nm.3394](https://doi.org/10.1038/nm.3394); pmid: [24202395](https://pubmed.ncbi.nlm.nih.gov/24202395/)
- M. R. Junttila, F. J. de Sauvage, Influence of tumour micro-environment heterogeneity on therapeutic response. *Nature* **501**, 346–354 (2013). doi: [10.1038/nature12626](https://doi.org/10.1038/nature12626); pmid: [24048067](https://pubmed.ncbi.nlm.nih.gov/24048067/)
- R. Stupp et al., Radiotherapy plus concomitant and adjuvant temozolomide for glioblastoma. *N. Engl. J. Med.* **352**, 987–996 (2005). doi: [10.1056/NEJMoa043330](https://doi.org/10.1056/NEJMoa043330); pmid: [15758009](https://pubmed.ncbi.nlm.nih.gov/15758009/)
- Y. Komohara, K. Ohnishi, J. Kuratsu, M. Takeya, Possible involvement of the M2 anti-inflammatory macrophage phenotype in growth of human gliomas. *J. Pathol.* **216**, 15–24 (2008). doi: [10.1002/path.2370](https://doi.org/10.1002/path.2370); pmid: [18553315](https://pubmed.ncbi.nlm.nih.gov/18553315/)
- L. Bingle, N. J. Brown, C. E. Lewis, The role of tumour-associated macrophages in tumour progression: Implications for new anticancer therapies. *J. Pathol.* **196**, 254–265 (2002). doi: [10.1002/path.1027](https://doi.org/10.1002/path.1027); pmid: [11857487](https://pubmed.ncbi.nlm.nih.gov/11857487/)
- S. F. Hussain et al., The role of human glioma-infiltrating microglia/macrophages in mediating antitumor immune responses. *Neuro-oncol.* **8**, 261–279 (2006). doi: [10.1215/15228517-2006-008](https://doi.org/10.1215/15228517-2006-008); pmid: [16775224](https://pubmed.ncbi.nlm.nih.gov/16775224/)
- B. Ruffell, L. M. Coussens, Macrophages and therapeutic resistance in cancer. *Cancer Cell* **27**, 462–472 (2015). doi: [10.1016/j.ccr.2015.02.015](https://doi.org/10.1016/j.ccr.2015.02.015); pmid: [25858805](https://pubmed.ncbi.nlm.nih.gov/25858805/)
- S. M. Pyonteck et al., CSF-1R inhibition alters macrophage polarization and blocks glioma progression. *Nat. Med.* **19**, 1264–1272 (2013). doi: [10.1038/nm.3337](https://doi.org/10.1038/nm.3337); pmid: [24056773](https://pubmed.ncbi.nlm.nih.gov/24056773/)
- S. J. Coniglio et al., Microglial stimulation of glioblastoma invasion involves epidermal growth factor receptor (EGFR) and colony stimulating factor 1 receptor (CSF-1R) signaling. *Mol. Med.* **18**, 519–527 (2012). doi: [10.2119/molmed.2011.00217](https://doi.org/10.2119/molmed.2011.00217); pmid: [22294205](https://pubmed.ncbi.nlm.nih.gov/22294205/)
- S. Patel, M. R. Player, Colony-stimulating factor-1 receptor inhibitors for the treatment of cancer and inflammatory disease. *Curr. Top. Med. Chem.* **9**, 599–610 (2009). doi: [10.2174/156802609789007327](https://doi.org/10.2174/156802609789007327); pmid: [19689368](https://pubmed.ncbi.nlm.nih.gov/19689368/)
- C. H. Ries et al., Targeting tumor-associated macrophages with anti-CSF-1R antibody reveals a strategy for cancer therapy. *Cancer Cell* **25**, 846–859 (2014). doi: [10.1016/j.ccr.2014.05.016](https://doi.org/10.1016/j.ccr.2014.05.016); pmid: [24898549](https://pubmed.ncbi.nlm.nih.gov/24898549/)
- W. D. Tap et al., Structure-guided blockade of CSF1R kinase in tenosynovial giant-cell tumor. *N. Engl. J. Med.* **373**, 428–437 (2015). doi: [10.1056/NEJMoa1411366](https://doi.org/10.1056/NEJMoa1411366); pmid: [26222558](https://pubmed.ncbi.nlm.nih.gov/26222558/)
- D. Hambardzumyan, N. M. Amankulor, K. Y. Helmy, O. J. Becher, E. C. Holland, Modeling adult gliomas using RCAS/t-va technology. *Transl. Oncol.* **2**, 89–95 (2009). doi: [10.1593/tlo.09100](https://doi.org/10.1593/tlo.09100); pmid: [19412424](https://pubmed.ncbi.nlm.nih.gov/19412424/)
- S. Hanzelmann, R. Castelo, J. Guinney, GSEA: Gene set variation analysis for microarray and RNA-seq data. *BMC Bioinformatics* **14**, 7 (2013). doi: [10.1186/1471-2105-14-7](https://doi.org/10.1186/1471-2105-14-7); pmid: [23323831](https://pubmed.ncbi.nlm.nih.gov/23323831/)
- S. M. Brachmann et al., Characterization of the mechanism of action of the pan class I PI3K inhibitor NVP-BKM120 across a broad range of concentrations. *Mol. Cancer Ther.* **11**, 1747–1757 (2012). doi: [10.1158/1535-7163.MCT-11-1021](https://doi.org/10.1158/1535-7163.MCT-11-1021); pmid: [22653967](https://pubmed.ncbi.nlm.nih.gov/22653967/)
- C. W. Brennan et al., The somatic genomic landscape of glioblastoma. *Cell* **155**, 462–477 (2013). doi: [10.1016/j.cell.2013.09.034](https://doi.org/10.1016/j.cell.2013.09.034); pmid: [24120142](https://pubmed.ncbi.nlm.nih.gov/24120142/)
- P. Therasse et al., New guidelines to evaluate the response to treatment in solid tumors. *J. Natl. Cancer Inst.* **92**, 205–216 (2000). doi: [10.1093/jnci/92.3.205](https://doi.org/10.1093/jnci/92.3.205); pmid: [10655437](https://pubmed.ncbi.nlm.nih.gov/10655437/)
- J. E. Burda, M. V. Sofroniew, Reactive gliosis and the multicellular response to CNS damage and disease. *Neuron* **81**, 229–248 (2014). doi: [10.1016/j.neuron.2013.12.034](https://doi.org/10.1016/j.neuron.2013.12.034); pmid: [24462092](https://pubmed.ncbi.nlm.nih.gov/24462092/)
- E. N. Arwert, E. Hoste, F. M. Watt, Epithelial stem cells, wound healing and cancer. *Nat. Rev. Cancer* **12**, 170–180 (2012). doi: [10.1038/nrc3217](https://doi.org/10.1038/nrc3217); pmid: [22362215](https://pubmed.ncbi.nlm.nih.gov/22362215/)
- F. Ginhoux, J. L. Schultze, P. J. Murray, J. Ochando, S. K. Biswas, New insights into the multidimensional concept of macrophage ontogeny, activation and function. *Nat. Immunol.* **17**, 34–40 (2016). doi: [10.1038/ni.3324](https://doi.org/10.1038/ni.3324); pmid: [26681460](https://pubmed.ncbi.nlm.nih.gov/26681460/)
- R. L. Bowman, J. A. Joyce, Therapeutic targeting of tumor-associated macrophages and microglia in glioblastoma. *Immunotherapy* **6**, 663–666 (2014). doi: [10.2217/mt.14.48](https://doi.org/10.2217/mt.14.48); pmid: [25041027](https://pubmed.ncbi.nlm.nih.gov/25041027/)
- G. Locatelli et al., Primary oligodendrocyte death does not elicit anti-CNS immunity. *Nat. Neurosci.* **15**, 543–550 (2012). doi: [10.1038/nn.3062](https://doi.org/10.1038/nn.3062); pmid: [22366759](https://pubmed.ncbi.nlm.nih.gov/22366759/)
- K. Gabrusiewicz et al., Characteristics of the alternative phenotype of microglia/macrophages and its modulation in experimental gliomas. *PLOS ONE* **6**, e23902 (2011). doi: [10.1371/journal.pone.0023902](https://doi.org/10.1371/journal.pone.0023902); pmid: [21901144](https://pubmed.ncbi.nlm.nih.gov/21901144/)
- J. D. Sedgwick et al., Isolation and direct characterization of resident microglial cells from the normal and inflamed central nervous system. *Proc. Natl. Acad. Sci. U.S.A.* **88**, 7438–7442 (1991). doi: [10.1073/pnas.88.16.7438](https://doi.org/10.1073/pnas.88.16.7438); pmid: [1651506](https://pubmed.ncbi.nlm.nih.gov/1651506/)
- F. Kratochvill et al., TNF counterbalances the emergence of M2 tumor macrophages. *Cell Reports* **12**, 1902–1914 (2015). doi: [10.1016/j.celrep.2015.08.033](https://doi.org/10.1016/j.celrep.2015.08.033); pmid: [26365184](https://pubmed.ncbi.nlm.nih.gov/26365184/)
- S. K. Biswas, A. Mantovani, Macrophage plasticity and interaction with lymphocyte subsets: Cancer as a paradigm. *Nat. Immunol.* **11**, 889–896 (2010). doi: [10.1038/ni.1937](https://doi.org/10.1038/ni.1937); pmid: [20856220](https://pubmed.ncbi.nlm.nih.gov/20856220/)
- R. Ostuni et al., Latent enhancers activated by stimulation in differentiated cells. *Cell* **152**, 157–171 (2013). doi: [10.1016/j.cell.2012.12.018](https://doi.org/10.1016/j.cell.2012.12.018); pmid: [23332752](https://pubmed.ncbi.nlm.nih.gov/23332752/)
- D. M. Mosser, J. P. Edwards, Exploring the full spectrum of macrophage activation. *Nat. Rev. Immunol.* **8**, 958–969 (2008). doi: [10.1038/nri2448](https://doi.org/10.1038/nri2448); pmid: [19029990](https://pubmed.ncbi.nlm.nih.gov/19029990/)
- A. Mantovani, S. K. Biswas, M. R. Galdiero, A. Sica, M. Locati, Macrophage plasticity and polarization in tissue repair and remodelling. *J. Pathol.* **229**, 176–185 (2013). doi: [10.1002/path.4133](https://doi.org/10.1002/path.4133); pmid: [23096265](https://pubmed.ncbi.nlm.nih.gov/23096265/)
- B. J. Falser, R. A. Macsata, D. Plummer, L. Mishra, A. N. Sidawy, Transforming growth factor- β and wound healing. *Perspect. Vasc. Surg. Endovasc. Ther.* **18**, 55–62 (2006). doi: [10.1177/153100350601800123](https://doi.org/10.1177/153100350601800123); pmid: [16628336](https://pubmed.ncbi.nlm.nih.gov/16628336/)
- J. Silver, J. H. Miller, Regeneration beyond the glial scar. *Nat. Rev. Neurosci.* **5**, 146–156 (2004). doi: [10.1038/nrn1326](https://doi.org/10.1038/nrn1326); pmid: [14735117](https://pubmed.ncbi.nlm.nih.gov/14735117/)
- F. E. Lund, B. A. Garvy, T. D. Randall, D. P. Harris, Regulatory roles for cytokine-producing B cells in infection and autoimmune disease. *Curr. Dir. Autoimmun.* **8**, 25–54 (2005). doi: [10.1159/000082086](https://doi.org/10.1159/000082086); pmid: [15564716](https://pubmed.ncbi.nlm.nih.gov/15564716/)
- D. P. Harris et al., Reciprocal regulation of polarized cytokine production by effector B and T cells. *Nat. Immunol.* **1**, 475–482 (2000). doi: [10.1038/82717](https://doi.org/10.1038/82717); pmid: [11101868](https://pubmed.ncbi.nlm.nih.gov/11101868/)
- B. Johansson-Lindbom, C. A. Borrebaeck, Germinal center B cells constitute a predominant physiological source of IL-4: Implication for Th2 development in vivo. *J. Immunol.* **168**, 3165–3172 (2002). doi: [10.4049/jimmunol.168.7.3165](https://doi.org/10.4049/jimmunol.168.7.3165); pmid: [11907068](https://pubmed.ncbi.nlm.nih.gov/11907068/)
- O. Butovsky, A. E. Talpalar, K. Ben-Yaakov, M. Schwartz, Activation of microglia by aggregated beta-amyloid or lipopolysaccharide impairs MHC-II expression and renders them cytotoxic whereas IFN- γ and IL-4 render them protective. *Mol. Cell. Neurosci.* **29**, 381–393 (2005). doi: [10.1016/j.jmcc.2005.03.005](https://doi.org/10.1016/j.jmcc.2005.03.005); pmid: [15890528](https://pubmed.ncbi.nlm.nih.gov/15890528/)
- S. J. Forbes, N. Rosenthal, Preparing the ground for tissue regeneration: From mechanism to therapy. *Nat. Med.* **20**, 857–869 (2014). doi: [10.1038/nm.3653](https://doi.org/10.1038/nm.3653); pmid: [25100531](https://pubmed.ncbi.nlm.nih.gov/25100531/)
- M. W. Wynes, D. W. Riches, Induction of macrophage insulin-like growth factor-I expression by the Th2 cytokines IL-4 and IL-13. *J. Immunol.* **171**, 3550–3559 (2003). doi: [10.4049/jimmunol.171.7.3550](https://doi.org/10.4049/jimmunol.171.7.3550); pmid: [14500651](https://pubmed.ncbi.nlm.nih.gov/14500651/)
- B. K. Kaspar, J. Lladó, N. Sherkat, J. D. Rothstein, F. H. Gage, Retrograde viral delivery of IGF-1 prolongs survival in a mouse ALS model. *Science* **301**, 839–842 (2003). doi: [10.1126/science.1086137](https://doi.org/10.1126/science.1086137); pmid: [12907804](https://pubmed.ncbi.nlm.nih.gov/12907804/)
- W. H. Zheng, S. Kar, S. Doré, R. Quirion, Insulin-like growth factor-1 (IGF-1): A neuroprotective trophic factor acting via the Akt kinase pathway. *J. Neural Transm. Suppl.* **2000**, 261–272 (2000). pmid: [11205145](https://pubmed.ncbi.nlm.nih.gov/11205145/)
- S. Dupraz et al., The insulin-like growth factor 1 receptor is essential for axonal regeneration in adult central nervous system neurons. *PLOS ONE* **8**, e54462 (2013). doi: [10.1371/journal.pone.0054462](https://doi.org/10.1371/journal.pone.0054462); pmid: [23349896](https://pubmed.ncbi.nlm.nih.gov/23349896/)
- A. M. Fernandez, I. Torres-Alemán, The many faces of insulin-like peptide signalling in the brain. *Nat. Rev. Neurosci.* **13**, 225–239 (2012). doi: [10.1038/nrn3209](https://doi.org/10.1038/nrn3209); pmid: [22430016](https://pubmed.ncbi.nlm.nih.gov/22430016/)
- M. Pollak, Insulin and insulin-like growth factor signalling in neoplasia. *Nat. Rev. Cancer* **8**, 915–928 (2008). doi: [10.1038/nrc2536](https://doi.org/10.1038/nrc2536); pmid: [19029956](https://pubmed.ncbi.nlm.nih.gov/19029956/)
- A. Liberzon et al., The Molecular Signatures Database (MSigDB) hallmark gene set collection. *Cell Syst.* **1**, 417–425 (2015). doi: [10.1016/j.cels.2015.12.004](https://doi.org/10.1016/j.cels.2015.12.004); pmid: [26771021](https://pubmed.ncbi.nlm.nih.gov/26771021/)
- A. Murat et al., Modulation of angiogenic and inflammatory response in glioblastoma by hypoxia. *PLOS ONE* **4**, e5947 (2009). doi: [10.1371/journal.pone.0005947](https://doi.org/10.1371/journal.pone.0005947); pmid: [19536297](https://pubmed.ncbi.nlm.nih.gov/19536297/)
- N. Herrmann-Kleiter, G. Baier, NFAT pulls the strings during CD4⁺ T helper cell effector functions. *Blood* **115**, 2989–2997 (2010). doi: [10.1182/blood-2009-10-233585](https://doi.org/10.1182/blood-2009-10-233585); pmid: [21013781](https://pubmed.ncbi.nlm.nih.gov/21013781/)
- N. Butowski et al., Orally administered colony stimulating factor 1 receptor inhibitor PLX3397 in recurrent glioblastoma: An Ivy Foundation Early Phase Clinical Trials Consortium phase II study. *Neuro-oncol.* **18**, 557–564 (2016). doi: [10.1093/neuonc/nov245](https://doi.org/10.1093/neuonc/nov245); pmid: [26449250](https://pubmed.ncbi.nlm.nih.gov/26449250/)
- C. Holohan, S. Van Schaeybroeck, D. B. Longley, P. G. Johnston, Cancer drug resistance: An evolving paradigm. *Nat. Rev. Cancer* **13**, 714–726 (2013). doi: [10.1038/nrc3599](https://doi.org/10.1038/nrc3599); pmid: [24060863](https://pubmed.ncbi.nlm.nih.gov/24060863/)
- M. J. Mulvihill et al., Discovery of OSI-906: A selective and orally efficacious dual inhibitor of the IGF-1 receptor and insulin receptor. *Future Med. Chem.* **1**, 1153–1171 (2009). doi: [10.4155/fmc.09.89](https://doi.org/10.4155/fmc.09.89); pmid: [21425998](https://pubmed.ncbi.nlm.nih.gov/21425998/)
- M. H. Roehrl et al., Selective inhibition of calcineurin-NFAT signaling by blocking protein-protein interaction with small organic molecules. *Proc. Natl. Acad. Sci. U.S.A.* **101**, 7554–7559 (2004). doi: [10.1073/pnas.0401835101](https://doi.org/10.1073/pnas.0401835101); pmid: [15131267](https://pubmed.ncbi.nlm.nih.gov/15131267/)
- K. Loser et al., FK506 controls CD40L-induced systemic autoimmunity in mice. *J. Invest. Dermatol.* **126**, 1307–1315 (2006). doi: [10.1038/sj.jid.5700185](https://doi.org/10.1038/sj.jid.5700185); pmid: [16470176](https://pubmed.ncbi.nlm.nih.gov/16470176/)
- Y. Chiba, M. Todoroki, Y. Nishida, M. Tanabe, M. Misawa, A novel STAT6 inhibitor AS1517499 ameliorates antigen-induced bronchial hypercontractility in mice. *Am. J. Respir. Cell Mol. Biol.* **41**, 516–524 (2009). doi: [10.1165/rmb.2008-01630C](https://doi.org/10.1165/rmb.2008-01630C); pmid: [19202006](https://pubmed.ncbi.nlm.nih.gov/19202006/)
- C. Dai et al., PDGF autocrine stimulation dedifferentiates cultured astrocytes and induces oligodendrogliomas and oligoastrocytomas from neural progenitors and astrocytes in vivo. *Genes Dev.* **15**, 1913–1925 (2001). doi: [10.1101/gad.903001](https://doi.org/10.1101/gad.903001); pmid: [11485986](https://pubmed.ncbi.nlm.nih.gov/11485986/)
- E. Tchougounova et al., Loss of Arf causes tumor progression of PDGFB-induced oligodendroglioma. *Oncogene* **26**, 6289–6296 (2007). doi: [10.1038/sj.onc.1210455](https://doi.org/10.1038/sj.onc.1210455); pmid: [17438529](https://pubmed.ncbi.nlm.nih.gov/17438529/)
- T. Ozawa et al., Most human non-GIMP glioblastoma subtypes evolve from a common proneural-like precursor glioma. *Cancer Cell* **26**, 288–300 (2014). doi: [10.1016/j.ccr.2014.06.005](https://doi.org/10.1016/j.ccr.2014.06.005); pmid: [25117714](https://pubmed.ncbi.nlm.nih.gov/25117714/)
- M. Squatrito et al., Loss of ATM/Chk2/p53 pathway components accelerates tumor development and contributes to radiation resistance in gliomas. *Cancer Cell* **18**, 619–629 (2010). doi: [10.1016/j.ccr.2010.10.034](https://doi.org/10.1016/j.ccr.2010.10.034); pmid: [21156285](https://pubmed.ncbi.nlm.nih.gov/21156285/)
- X. Hu et al., mTOR promotes survival and astrocytic characteristics induced by Pten/AKT signaling in glioblastoma. *Neoplasia* **7**, 356–368 (2005). doi: [10.1593/neo.04595](https://doi.org/10.1593/neo.04595); pmid: [15967113](https://pubmed.ncbi.nlm.nih.gov/15967113/)
- J. T. Huse et al., The PTEN-regulating microRNA miR-26a is amplified in high-grade glioma and facilitates gliomagenesis in vivo. *Genes Dev.* **23**, 1327–1337 (2009). doi: [10.1101/gad.1777409](https://doi.org/10.1101/gad.1777409); pmid: [19487573](https://pubmed.ncbi.nlm.nih.gov/19487573/)
- A. H. Shih et al., Dose-dependent effects of platelet-derived growth factor-B on glial tumorigenesis. *Cancer Res.* **64**, 4783–4789 (2004). doi: [10.1158/0008-5472.CAN-03-3831](https://doi.org/10.1158/0008-5472.CAN-03-3831); pmid: [15256447](https://pubmed.ncbi.nlm.nih.gov/15256447/)
- J. B. Jensen, M. Parmar, Strengths and limitations of the neurosphere culture system. *Mol. Neurobiol.* **34**, 153–161 (2006). doi: [10.1385/MN.34.3.153](https://doi.org/10.1385/MN.34.3.153); pmid: [17308349](https://pubmed.ncbi.nlm.nih.gov/17308349/)
- N. J. Szerlip et al., Intratumoral heterogeneity of receptor tyrosine kinases EGFR and PDGFRA amplification in glioblastoma defines subpopulations with distinct growth factor response. *Proc. Natl. Acad. Sci. U.S.A.* **109**, 3041–3046 (2012). doi: [10.1073/pnas.1114033109](https://doi.org/10.1073/pnas.1114033109); pmid: [22323597](https://pubmed.ncbi.nlm.nih.gov/22323597/)
- V. Ponomarev et al., A novel triple-modality reporter gene for whole-body fluorescent, bioluminescent, and nuclear noninvasive imaging. *Eur. J. Nucl. Med. Mol. Imaging* **31**, 740–751 (2004). doi: [10.1007/s00259-003-1441-5](https://doi.org/10.1007/s00259-003-1441-5); pmid: [15014901](https://pubmed.ncbi.nlm.nih.gov/15014901/)
- M. Serrano et al., Role of the INK4a locus in tumor suppression and cell mortality. *Cell* **85**, 27–37 (1996). doi: [10.1016/S0092-8674\(00\)81079-X](https://doi.org/10.1016/S0092-8674(00)81079-X); pmid: [8620534](https://pubmed.ncbi.nlm.nih.gov/8620534/)
- D. N. Louis et al., The 2007 WHO classification of tumors of the central nervous system. *Acta Neuropathol.* **114**,

- 97–109 (2007). doi: [10.1007/s00401-007-0243-4](https://doi.org/10.1007/s00401-007-0243-4); pmid: [17618441](https://pubmed.ncbi.nlm.nih.gov/17618441/)
64. D. C. Allred, J. M. Harvey, M. Berardo, G. M. Clark, Prognostic and predictive factors in breast cancer by immunohistochemical analysis. *Mod. Pathol.* **11**, 155–168 (1998). pmid: [9504686](https://pubmed.ncbi.nlm.nih.gov/9504686/)
65. V. E. Seshan, A. Olshen, DNACopy: DNA copy number data analysis. R package version 1.44.0.
66. A. Dobin *et al.*, STAR: Ultrafast universal RNA-seq aligner. *Bioinformatics* **29**, 15–21 (2013). doi: [10.1093/bioinformatics/bts635](https://doi.org/10.1093/bioinformatics/bts635); pmid: [23104886](https://pubmed.ncbi.nlm.nih.gov/23104886/)
67. H. Li *et al.*, The Sequence Alignment/Map format and SAMtools. *Bioinformatics* **25**, 2078–2079 (2009). doi: [10.1093/bioinformatics/btp352](https://doi.org/10.1093/bioinformatics/btp352); pmid: [19505943](https://pubmed.ncbi.nlm.nih.gov/19505943/)
68. S. Anders, P. T. Pyl, W. Huber, HTSeq—A Python framework to work with high-throughput sequencing data. *Bioinformatics* **31**, 166–169 (2015). doi: [10.1093/bioinformatics/btu638](https://doi.org/10.1093/bioinformatics/btu638); pmid: [25260700](https://pubmed.ncbi.nlm.nih.gov/25260700/)
69. C. W. Law, Y. Chen, W. Shi, G. K. Smyth, voom: Precision weights unlock linear model analysis tools for RNA-seq read counts. *Genome Biol.* **15**, R29 (2014). doi: [10.1186/gb-2014-15-2-r29](https://doi.org/10.1186/gb-2014-15-2-r29); pmid: [24485249](https://pubmed.ncbi.nlm.nih.gov/24485249/)
70. G. Dennis Jr. *et al.*, DAVID: Database for Annotation, Visualization, and Integrated Discovery. *Genome Biol.* **4**, 3 (2003). doi: [10.1186/gb-2003-4-5-p3](https://doi.org/10.1186/gb-2003-4-5-p3); pmid: [12734009](https://pubmed.ncbi.nlm.nih.gov/12734009/)
71. A. Subramanian *et al.*, Gene set enrichment analysis: A knowledge-based approach for interpreting genome-wide expression profiles. *Proc. Natl. Acad. Sci. U.S.A.* **102**, 15545–15550 (2005). doi: [10.1073/pnas.0506580102](https://doi.org/10.1073/pnas.0506580102); pmid: [16199517](https://pubmed.ncbi.nlm.nih.gov/16199517/)
72. P. J. Balwierz *et al.*, ISMARA: Automated modeling of genomic signals as a democracy of regulatory motifs. *Genome Res.* **24**, 869–884 (2014). doi: [10.1101/gr.169508.113](https://doi.org/10.1101/gr.169508.113); pmid: [24515121](https://pubmed.ncbi.nlm.nih.gov/24515121/)
73. M. Setty *et al.*, Inferring transcriptional and microRNA-mediated regulatory programs in glioblastoma. *Mol. Syst. Biol.* **8**, 605 (2012). doi: [10.1038/msb.2012.37](https://doi.org/10.1038/msb.2012.37); pmid: [22929615](https://pubmed.ncbi.nlm.nih.gov/22929615/)
74. M. Pachkov, I. Erb, N. Molina, E. van Nimwegen, SwissRegulon: A database of genome-wide annotations of regulatory sites. *Nucleic Acids Res.* **35** (Database), D127–D131 (2007). doi: [10.1093/nar/gkl857](https://doi.org/10.1093/nar/gkl857); pmid: [17130146](https://pubmed.ncbi.nlm.nih.gov/17130146/)
75. J. Friedman, T. Hastie, R. Tibshirani, Regularization paths for generalized linear models via coordinate descent. *J. Stat. Softw.* **33**, 1–22 (2010). doi: [10.18637/jss.v033.i01](https://doi.org/10.18637/jss.v033.i01); pmid: [20808728](https://pubmed.ncbi.nlm.nih.gov/20808728/)
76. Y. Zhu, P. Qiu, Y. Ji, TCGA-assembler: Open-source software for retrieving and processing TCGA data. *Nat. Methods* **11**, 599–600 (2014). doi: [10.1038/nmeth.2956](https://doi.org/10.1038/nmeth.2956); pmid: [24874569](https://pubmed.ncbi.nlm.nih.gov/24874569/)
77. H. Wickham, *ggplot2: Elegant Graphics for Data Analysis* (Springer, 2009).
78. S. Epskamp, A. O. J. Cramer, L. J. Waldorp, V. D. Schmittmann, D. Borsboom, qgraph: Network visualizations of relationships in psychometric data. *J. Stat. Softw.* **48**, 1–18 (2012). doi: [10.18637/jss.v048.i04](https://doi.org/10.18637/jss.v048.i04)

ACKNOWLEDGMENTS

We thank X. Chen and N. Shah for excellent technical support. We are grateful to C. Brennan for generously providing the TSS73 patient tumorsphere line. We thank R. Benezra for critically reading the manuscript and O. Olson, P. Castel, and S. Schwartz for experimental advice. We thank the Animal Imaging Core, the Antitumor Assessment Core, Flow Cytometry Core, and Integrated Genomics Operation at MSKCC for assistance. The data presented in this manuscript are tabulated in the main paper and in the supplementary materials. All sequencing data has been deposited to the GEO under accession no. GSE69104, and aCGH data under accession number GSE80399. BLZ945 is available from Novartis under a material transfer agreement with J.C.S., Novartis, D.F.Q., R.L.B., and J.A.J. are inventors on a patent application filed by MSKCC related to the use of combination therapies with CSF-1R inhibitors for gliomas. This research was supported by the U.S. National Cancer Institute (NCI) (R01CA148967, J.A.J.), the Ludwig Institute for Cancer Research (J.A.J.), fellowships from Canadian Institutes of Health Research (D.F.Q.), NCI (F31CA167863, R.L.B.), American Brain Tumor Association (L.A.), Obra Social Ibercaja (A.J.S.), and the MSKCC Support Grant from the NCI (P30 CA008748).

SUPPLEMENTARY MATERIALS

www.sciencemag.org/content/352/6288/aad3018/suppl/DC1
Supplementary Text
Figs. S1 to S13
Tables S1 to S4

18 September 2015; accepted 8 April 2016
10.1126/science.aad3018



The tumor microenvironment underlies acquired resistance to CSF-1R inhibition in gliomas

Daniela F. Quail, Robert L. Bowman, Leila Akkari, Marsha L. Quick, Alberto J. Schuhmacher, Jason T. Huse, Eric C. Holland, James C. Sutton and Johanna A. Joyce (May 19, 2016)
Science **352** (6288), . [doi: 10.1126/science.aad3018]

Editor's Summary

Another pathway to cancer resistance

Therapies targeting the tumor microenvironment show promise for treating cancer. For example, antibodies targeting colony-stimulating factor-1 receptor (CSF-1R) inhibit protumorigenic macrophages and regress tumors in mouse models of glioblastoma multiforme (GBM), a deadly form of brain cancer. Quail *et al.* found that although CSF-1R blockade prolonged survival in mouse models of GBM, more than 50% of tumors eventually recurred. Recurrence was correlated with elevated PI3-K activity in tumors, driven by macrophage-secreted IGF-1. Blocking PI3-K and IGF-1 signaling in rebounding tumors prolonged survival. Thus, tumors can acquire resistance to therapy through intrinsic changes and through changes in their microenvironment.

Science, this issue p. 10.1126/science.aad3018

This copy is for your personal, non-commercial use only.

Article Tools Visit the online version of this article to access the personalization and article tools:
<http://science.sciencemag.org/content/352/6288/aad3018>

Permissions Obtain information about reproducing this article:
<http://www.sciencemag.org/about/permissions.dtl>

Science (print ISSN 0036-8075; online ISSN 1095-9203) is published weekly, except the last week in December, by the American Association for the Advancement of Science, 1200 New York Avenue NW, Washington, DC 20005. Copyright 2016 by the American Association for the Advancement of Science; all rights reserved. The title *Science* is a registered trademark of AAAS.